

Linear stability of an oceanic front at finite Rossby number

Subhajit Kar^{1†}, Roy Barkan^{1,2} and John R. Taylor³

¹Porter School of the Environment and Earth Sciences, Tel Aviv University, Tel Aviv 69978, Israel

²Department of Atmospheric and Oceanic Sciences, University of California, Los Angeles, CA, USA

³DAMTP, University of Cambridge, Centre for Mathematical Sciences, Wilberforce Road, Cambridge CB3 0WA, UK.

(Received xx; revised xx; accepted xx)

Submesoscale currents in the ocean's mixed layer (ML), consisting of fronts, eddies, and filaments, are characterized by $\mathcal{O}(1)$ Rossby (Ro) and Richardson (Ri) numbers. These currents play a crucial role in mediating vertical exchange between the surface and ocean interior and in facilitating cross-scale energy transfers. Despite a growing understanding of their generation mechanisms and energy pathways, two fundamental questions remain unresolved - how does a finite Ro modify the dynamics of ML instabilities, and what mechanisms are responsible for ML frontal arrest when $Ro \sim \mathcal{O}(1)$. In this study, we address these questions through a linear stability analysis of a two-dimensional, geostrophically adjusted oceanic front based on the analytical model of Ou (1984), which allows systematic exploration across a range of Ro . In the low Ro , $Ri \sim \mathcal{O}(1)$ regime, the most unstable mode is that of baroclinic instability, with the buoyancy flux serving as the primary source of perturbation kinetic energy. As Ro increases, the dominant instability becomes an inertia-critical layer type, characterized by a resonant interaction between a Rossby wave and an inertia-gravity wave. In the $Ro \sim \mathcal{O}(1)$ regime, the shear production terms become comparable to the buoyancy flux term and even dominate in the region where the adjusted front is strongest. Our results suggest that shear production should be included in parameterizations of ML instabilities.

1. Introduction

Surface submesoscale currents, comprising mixed layer eddies, fronts, and filaments, are pervasive features in the mixed layer (ML) of the upper ocean, exhibiting horizontal scales of $\mathcal{O}(0.1\text{--}10)$ km and temporal scales ranging from hours to days. These submesoscale currents are characterized by $\mathcal{O}(1)$ Rossby number $Ro (= U_0/fL_0)$ and Richardson number $Ri (= N^2H^2/U_0^2)$, where U_0 is a horizontal velocity scale, L_0 is a horizontal length scale, H is a vertical length scale, f is the Coriolis parameter, and N is the buoyancy frequency (McWilliams 2016). This distinguishes them from oceanic mesoscale eddies, which have horizontal scales of $\mathcal{O}(10\text{--}100)$ km and a timescale of many days, characterized by $Ro \ll 1$ and $Ri \gg 1$. Owing to their large vertical velocities, submesoscale currents are instrumental in mediating the exchange of momentum, heat, and tracers between the surface and the ocean interior, thereby modulating a broad spectrum of physical and biogeochemical processes (Thomas *et al.* 2008; Mahadevan 2016; Taylor & Thompson 2023).

Submesoscale currents are generated through several processes, including baroclinic mixed layer instabilities (MLIs; Boccaletti *et al.* 2007; Fox-Kemper *et al.* 2008), strain driven frontogenesis (Hoskins & Bretherton 1972), and frontogenesis induced by boundary layer turbulence (Gula *et al.* 2014; McWilliams *et al.* 2015; Dauhajre *et al.* 2025). These mechanisms contribute to the

† Email address for correspondence: subhajitkar@mail.tau.ac.il

restratification of the ML by releasing the available potential energy (APE) stored in horizontal density gradients, and to bidirectional cross-scale kinetic energy (KE) fluxes (Capet *et al.* 2008b; Balwada *et al.* 2022; Srinivasan *et al.* 2023). Specifically, finite-amplitude MLIs develop into mixed layer eddies (MLEs), which have been shown to exhibit an inverse KE cascade (Fox-Kemper *et al.* 2008). Consequently, KE is transferred upscale and can energize mesoscale eddies (Klein *et al.* 2019; Schubert *et al.* 2020; Srinivasan *et al.* 2023). In turn, mesoscale strain and boundary layer turbulence can initiate submesoscale frontogenesis (Barkan *et al.* 2019), thereby driving a forward KE flux that can deplete mesoscale KE (Srinivasan *et al.* 2023; Yu *et al.* 2024). The pathways of these forward KE fluxes to dissipation are ultimately determined by the processes that lead to frontal arrest. Under suitable forcing conditions, symmetric instability can emerge as the arrest mechanism (Thomas 2005); otherwise, horizontal shear instability becomes a likely candidate (Sullivan & McWilliams 2018).

Historically, the distinction between MLIs and classical baroclinic instability (BCI, Eady 1949) has been framed primarily in terms of the Richardson number, Ri , with MLIs typically associated with $Ri \sim \mathcal{O}(1)$ (figure 1). Most notably, Stone (1966, 1970, 1971) investigated non-geostrophic effects on BCI using Eady's framework. He found that as the Ri decreases, the wavelength of the most unstable mode increases while the growth rate diminishes relative to predictions from the quasigeostrophic (QG) approximation. The effects of horizontal shear on BCI have been studied in the QG regime by McIntyre (1970) and Gent (1974). They demonstrated that horizontal shear substantially alters the classical Eady problem by producing a counter-gradient horizontal momentum flux that stabilizes the BCI — a mechanism referred to as the barotropic governor (James 1987). In addition, cross-front variations in the mean flow were shown to spatially confine BCI modes in the cross-front direction (Ioannou & Lindzen 1986; Moore & Peltier 1987).

Moore & Peltier (1990) and Barth (1994) investigated the stability of a 2D front using the primitive equations in the $Ro \ll 1, Ri \gg 1$ regime. They identified two distinct instability modes - a long-wave mode and a short-wave mode. The long-wave instability mode closely resembles the classical Eady-type BCI and arises from the phase-locking of two counter-propagating Rossby waves (Hoskins *et al.* 1985). In contrast, the short-wave instability, absent in the QG approximation, can be viewed as a continuation of BCI, wherein one Rossby wave is replaced by an inertia-gravity wave (IGW). This instability mechanism involves a resonant interaction between a Rossby wave and an IGW and is commonly referred to as inertia-critical layer (ICL) instability (Stone 1970; Nakamura 1988).

The typical length scale of MLIs is estimated to lie within the range $4 \leq L_{\text{MLI}}/R \leq 6$ (Eldevik & Dysthe 2002; Özgökmen *et al.* 2011), where $L_{\text{MLI}} \approx 4R\sqrt{1+Ri^{-1}}$ represents the wavelength of the most unstable MLI mode (Stone 1966), R is the ML deformation radius, and H denotes the ML depth. Using the upper bound of this range (corresponding to $Ri = 0.8$), Dong *et al.* (2020) provided a global estimate of the MLI length scale in the ocean, finding a typical value of approximately 6 km at mid-latitudes. High-resolution realistic ocean simulations capable of resolving these scales indicate that the associated local Rossby number in such solutions is typically $\mathcal{O}(1)$ (e.g., Capet *et al.* 2008a; Barkan *et al.* 2017), implying that horizontal shear may have important effects on MLI dynamics. Furthermore, Bodner *et al.* (2023) recently revised the MLI-induced restratification parametrization originally developed by Fox-Kemper *et al.* (2008), incorporating an arrested frontal length scale derived from the theory of turbulent thermal wind (McWilliams *et al.* 2015). This suggests that MLIs are expected to also occur at spatial scales smaller than the ML deformation radius R , where the local Rossby number may be even larger and is expected to influence the growth rate and energetics of the instability. In addition, at these smaller scales, the finite Rossby number may potentially have important implications for frontal arrest mechanisms.

The preceding discussion motivates two fundamental open questions:

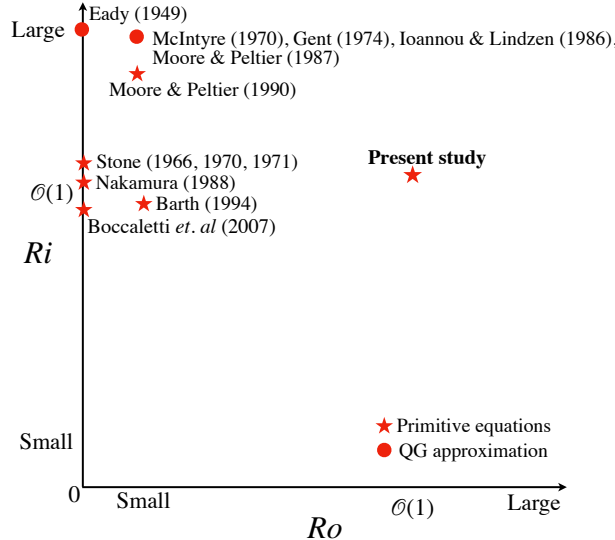


FIGURE 1. The parameter space examined by previous linear stability studies of baroclinic front configurations, shown schematically as a function of Rossby (Ro) and Richardson (Ri) numbers of the basic state. Here the Rossby number is defined in terms of the vertical relative vorticity of the basic state. In this study, the basic state allows us to specifically investigate the regime where $Ro \sim \mathcal{O}(1)$ and $Ri \sim \mathcal{O}(1)$.

- (i) how does a finite Ro affect the characteristics of MLI?
- (ii) what instability mechanisms can arrest submesoscale frontogenesis when $Ro \sim \mathcal{O}(1)$?

In this paper, we address these questions through a bi-global linear stability analysis (Theofilos 2011) of a geostrophically adjusted front. The classical frontal geostrophic adjustment problem describes the evolution of an isolated front, starting from a state of rest (Rossby 1937). At early times, a vertically sheared cross-front circulation develops in response to the difference between the hydrostatic pressure on each side of the front. As the flow evolves, the cross-front circulation drives frontogenesis, before the front adjusts to a geostrophically balanced state.

We consider a basic state based on the analytical solution of a geostrophically adjusted ML front as described by Ou (1984, herein after Ou84), enabling us to systematically explore stability properties across a range of Ro values that characterize the strength of the front. When Ro exceeds a critical value, $Ro > Ro_c$, the solutions exhibit a discontinuity, which makes the stability problem ill-posed. By considering smaller Rossby numbers with $Ro < Ro_c$, we seek instabilities that may act to equilibrate frontogenesis in the full time-dependent geostrophic adjustment problem.

We demonstrate that in the $Ro \ll 1$, $Ri \sim \mathcal{O}(1)$ regime, the adjusted front is unstable to BCI, and the growth rate of the most unstable mode closely matches the analytical solution of Stone (1971, herein after S71), with the buoyancy flux acting as the primary source of perturbation KE. In the oceanic submesoscale regime, characterized by $Ro \sim \mathcal{O}(1)$ and $Ri \sim \mathcal{O}(1)$, the most unstable growth rate remains comparable to that of S71, but the corresponding mode transitions to the ICL instability mode described above. In this regime, the buoyancy flux and the shear production terms contribute equally to the growth of the perturbation KE.

The paper is organized as follows. In §2, we discuss the basic-state configuration (§2.1) and the linear stability analysis (§2.2). Results of the stability analyses are shown in §3. In §4, we discuss the results and draw connections to the two open questions above. Finally, in §5, we summarize our findings.

2. Problem configuration

We perform a bi-global stability analysis of a 2D front in the (y, z) plane that is invariant in the along-front (x) direction. The dynamics are governed by the Boussinesq equations of motion for a rotating fluid under the f -plane approximation. To non-dimensionalize the governing equations, we follow the scaling proposed by Ou84. The length and time scales are,

$$x = R\hat{x}, \quad y = R\hat{y}, \quad z = H\hat{z}, \quad t = \frac{1}{f}\hat{t}, \quad (2.1a - c)$$

where the ‘hat’ describes a non-dimensional quantity, H is the ML depth, $R = \sqrt{\Delta B H}/f$ with ΔB is the buoyancy anomaly across the front, with the buoyancy $B = -g\rho/\rho_0$ (ρ is the flow density perturbation relative to the reference density ρ_0 , and g is the gravitational acceleration). The corresponding scales of the other flow fields are

$$U = fR\hat{U}, \quad V = fR\hat{V}, \quad W = fH\hat{W}, \quad P = f^2R^2\hat{P}, \quad B = (f^2R^2/H)\hat{B}, \quad (2.2a - d)$$

where \hat{U} , \hat{V} , and \hat{W} denote the non-dimensional velocity components in the x , y , and z directions, respectively; \hat{P} is the non-dimensional pressure, and \hat{B} is the non-dimensional buoyancy. To simplify notation, we omit the ‘hat’ symbol in the following analysis unless explicitly stated.

2.1. Basic state

The basic state is defined following Ou84, in which an initially motionless fluid with a lateral buoyancy gradient is geostrophically adjusted toward a balanced state, i.e., the along-front mean flow is in geostrophic balance with the lateral pressure gradient. For an imposed buoyancy profile $B(\eta)$, Ou84 derived the following solution for the along-front velocity U of the adjusted state,

$$y = \left(\frac{1}{2} - z\right) \frac{dB}{d\eta} + \eta, \quad (2.3a)$$

$$z = \left(\frac{d^2B}{d\eta^2}\right)^{-1} \left[1 + \frac{1}{2} \frac{d^2B}{d\eta^2} - \sqrt{\left(1 + \frac{1}{2} \frac{d^2B}{d\eta^2}\right)^2 - 2 \frac{d^2B}{d\eta^2} \xi} \right], \quad (2.3b)$$

$$U(y, z) = \left(\frac{1}{2} - z\right) \frac{dB}{d\eta}, \quad (2.3c)$$

where (η, ξ) denote the initial coordinates of a fluid particle that ends at (y, z) after geostrophic adjustment. In this study, we use

$$B(\eta) = -\frac{1}{2} \tanh(\beta\eta), \quad (2.4)$$

where β is a free parameter that measures the steepness of the initial buoyancy profile. Since the fluid is initially motionless and the prescribed buoyancy distribution (2.4) is depth-independent, the initial potential vorticity (PV) is zero. The geostrophic adjustment process conserves PV materially, and therefore, the PV of the adjusted front also remains zero. This is a physically relevant choice, as low PV typically characterizes oceanic ML fronts.

To characterize the frontal dynamics, we introduce a bulk Rossby number, Ro , defined in terms of the basic state velocity, U_0 , and frontal width, L_0 ,

$$Ro = \frac{U_0}{fL_0} = \frac{\beta^2}{4}, \quad (2.5)$$

where $U_0 = fR\beta/2$ (e.g., (2.3c)) and the typical dimensional cross-front length scale is $L_0 = 2R/\beta$ as noted above. Therefore, the non-dimensional frontal width, β , is linked with the Rossby number, and the dimensional cross-frontal width is $Ro^{-1/2}R$. The bulk Richardson number of

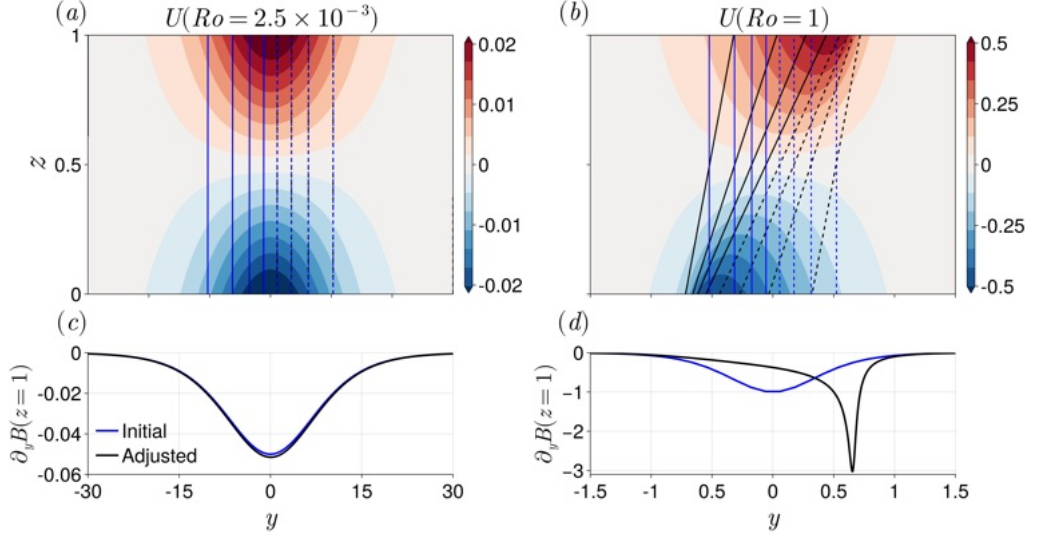


FIGURE 2. The solution of geostrophically adjusted ML front described by (2.3a–c) for (a) $Ro = 2.5 \times 10^{-3}$ and (b) $Ro = 1$. The blue (black) lines show the initial (adjusted) buoyancy contours with a contour interval of $B = 0.11$. Solid (dashed) lines denote positive (negative) values. Panels (c) and (d) show the initial (blue) and adjusted (black) horizontal buoyancy gradient $\partial_y B$ at the top surface ($z = 1$) corresponding to $Ro = 2.5 \times 10^{-3}$ and $Ro = 1$, respectively.

the front is defined as

$$Ri = \frac{N^2 H^2}{U_0^2} = 1, \quad (2.6)$$

where $N^2 = f^2 R^2 / H^2 |dy/dz| \beta / 2$ and $|dy/dz| = \beta / 2$ is the slope of the adjusted isopycnals (using 2.3a). This Ri number definition agrees with the local value computed from the frontal solutions ($Ri_\ell \equiv \partial_z B / (\partial_z U)^2 \sim \mathcal{O}(1)$; figures 3(c, d)).

For small Ro values, frontogenesis is relatively weak, resulting in minimal differences between the initial and adjusted buoyancy fields (see line contours in figure 2(a) and line plot in figure 2(c)). Consequently, the mean flow is nearly symmetric about $y = 0$ (see figures 2(a), 3(a)), with a local Rossby number $Ro_\ell (= -\partial_y U) \ll 1$. Additionally, weak frontogenesis results in weaker stratification and vertical shear, yielding a local Richardson number Ri_ℓ very close to 1. For large Ro values, geostrophic adjustment drives much stronger frontogenesis which leads to stronger horizontal buoyancy gradients near the top and bottom surfaces of the domain (line contours in figures 2(b, d)). The corresponding along-front mean flow is asymmetric about $y = 0$ (figure 2(b)), producing a pronounced asymmetry in the vorticity (figure 3(b)). In this regime, the frontal region is characterized by $|Ro_\ell| \sim \mathcal{O}(1)$ and $Ri_\ell \lesssim \mathcal{O}(1)$ (figures 3(b, d)) - characteristic of submesoscale oceanic fronts.

The necessary condition for instability of a baroclinic flow is a sign change in the isopycnal gradient of PV within the domain (Eliassen 1983). The adjusted front solution described by (2.3a – c) satisfies this condition for all Ro values considered (not shown), indicating that the basic state is susceptible to BCI.

2.2. Linear stability analysis

The solution described by (2.3a – c) breaks down when isopycnals intersect, i.e., when $\partial_y \eta = 0$. From (2.3(a)), (2.4), this occurs at the lower and upper surfaces of the domain when $|\partial_y^2 B| = 2$. We can therefore obtain non-singular solutions to (2.3a – c) when $\beta \lesssim 2.28$ (i.e., $Ro \lesssim 1.3$) and

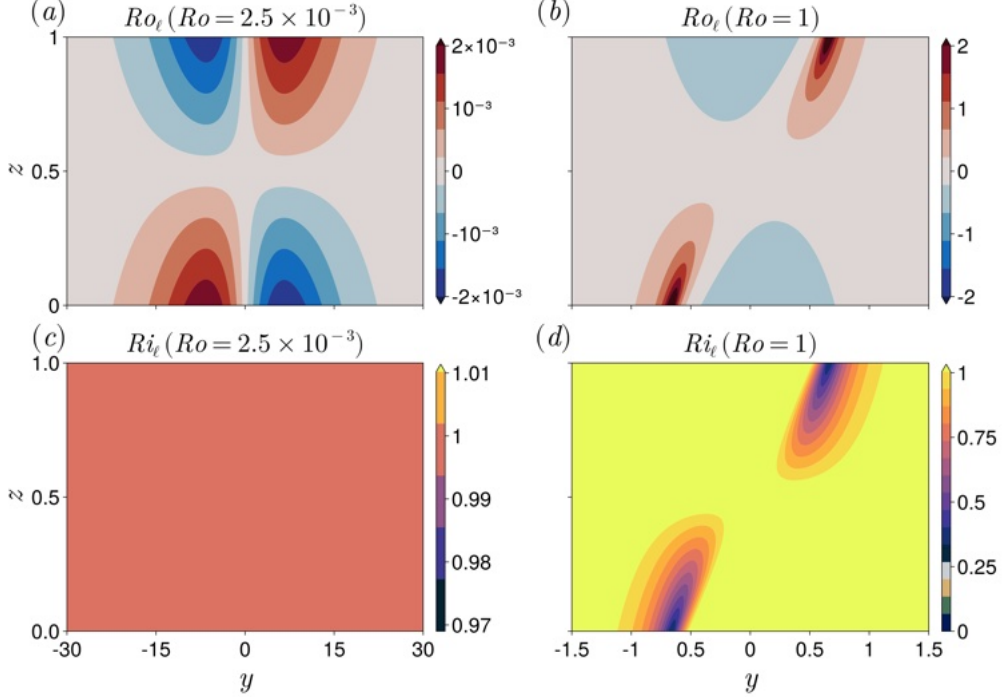


FIGURE 3. (a, b) The local Rossby number $Ro_\ell = -\partial_y U$ and (c, d) the local Richardson number $Ri_\ell = \partial_z B / (\partial_z U)^2$ of the mean flow shown in figures 2(a, b). In both cases, $Ri_\ell > 1/4$, therefore, the vertical shear of the mean flow is stable with respect to Miles-Howard criterion (Miles 1961).

perform a linear stability analysis in the range $2.5 \times 10^{-3} \leq Ro \leq 1$. To this end, we consider the evolution of infinitesimal perturbations to the geostrophically adjusted frontal flow described in §2.1. The resulting nondimensional, linearized Boussinesq equations of motion under the f -plane approximation are given by

$$\frac{D\mathbf{u}}{Dt} + \left(v \frac{\partial U}{\partial y} + w \frac{\partial U}{\partial z} \right) \hat{x} + \hat{z} \times \mathbf{u} = -\nabla p + \frac{1}{\epsilon} b \hat{z} + E \nabla^2 \mathbf{u}, \quad (2.7a)$$

$$\frac{Db}{Dt} + v \frac{\partial B}{\partial y} + w \frac{\partial B}{\partial z} = \frac{E}{Pr} \nabla^2 b, \quad (2.7b)$$

$$\nabla \cdot \mathbf{u} = 0, \quad (2.7c)$$

where $D/Dt \equiv \partial/\partial t + U(\partial/\partial x)$ is the material derivative, $\mathbf{u} \equiv (u, v, \epsilon w)$ is the velocity perturbation, $\epsilon = H/R$ is the aspect ratio, p is the pressure perturbation, and b is the buoyancy perturbation. The gradient and Laplacian operators are $\nabla \equiv (\partial/\partial x, \partial/\partial y, (1/\epsilon)\partial/\partial z)$, and $\nabla^2 \equiv \partial^2/\partial x^2 + \partial^2/\partial y^2 + (1/\epsilon^2)\partial^2/\partial z^2$. In what follows, we compare between hydrostatic and non-hydrostatic flow regimes by choosing $\epsilon = 0.1$ and $\epsilon = 1$, respectively. The Ekman number $E = \nu/fR^2$ is set to be 10^{-8} , and the Prandtl number $Pr = \nu/\kappa$ is taken to be 1. To eliminate pressure, following Teed *et al.* (2010), we apply the operator $\hat{z} \cdot \nabla \times \nabla \times$ and $\hat{z} \cdot \nabla \times$ to the momentum equation (2.7a). This procedure yields governing equations of three perturbation

variables, the vertical velocity w , the vertical vorticity ζ ($= \hat{z} \cdot \nabla \times \mathbf{u}$), and the buoyancy b ,

$$\begin{aligned} \frac{D}{Dt} \nabla^2 w + \left(\frac{\partial^2 U}{\partial y^2} - \frac{1}{\epsilon^2} \frac{\partial^2 U}{\partial z^2} \right) \frac{\partial w}{\partial x} + 2 \frac{\partial U}{\partial y} \left(\frac{\partial^2 w}{\partial x \partial y} - \frac{1}{\epsilon^2} \frac{\partial^2 v}{\partial x \partial z} \right) \\ - \frac{2}{\epsilon^2} \frac{\partial^2 U}{\partial y \partial z} \frac{\partial v}{\partial x} + \frac{1}{\epsilon^2} \frac{\partial \zeta}{\partial z} = \frac{1}{\epsilon^2} \nabla_h^2 b + E \nabla^4 w, \end{aligned} \quad (2.8a)$$

$$\frac{D\zeta}{Dt} + \frac{\partial U}{\partial y} \frac{\partial w}{\partial z} - \frac{\partial U}{\partial z} \frac{\partial w}{\partial y} - \frac{\partial^2 U}{\partial y \partial z} w - \frac{\partial^2 U}{\partial y^2} v - \frac{\partial w}{\partial z} = E \nabla^2 \zeta, \quad (2.8b)$$

$$\frac{Db}{Dt} + v \frac{\partial B}{\partial y} + w \frac{\partial B}{\partial z} = \frac{E}{Pr} \nabla^2 b, \quad (2.8c)$$

where $\nabla_h^2 \equiv \partial^2/\partial x^2 + \partial^2/\partial y^2$. The benefit of using (2.8(a–c)) over (2.7(a–c)) is that it enables us to examine the instability at an along-front wavenumber $k \rightarrow 0$. The horizontal velocities u and v are related to the vertical velocity w and vertical vorticity ζ by the identities,

$$\nabla_h^2 u = -\frac{\partial \zeta}{\partial y} - \frac{\partial^2 w}{\partial x \partial z}, \quad (2.9a)$$

$$\nabla_h^2 v = \frac{\partial \zeta}{\partial x} - \frac{\partial^2 w}{\partial y \partial z}. \quad (2.9b)$$

In deriving the above equations, we make use of the continuity equation (2.7c) and the definition of vertical vorticity ζ .

To facilitate comparison, we also perform QG stability analysis based on the same underlying frontal flow. The details of the QG stability setup are provided in Appendix D. In addition, we compare the stability results with the classical solutions of Eady (1949) and S71.

2.2.1. Normal mode equations

Next, we consider normal-mode perturbations of the form

$$[w, \zeta, b](x, y, z, t) = \Re([\tilde{w}, \tilde{\zeta}, \tilde{b}](y, z) e^{ikx+\sigma t}), \quad (2.10)$$

where the symbol \Re denotes the real part and a variable with ‘tilde’ denotes an eigenfunction. The variable $\sigma = \sigma_r + i\sigma_i$, where the real part σ_r , represents the growth rate, and the imaginary part σ_i , represents the frequency of the unstable perturbation.

After introducing the form (2.10) into the governing equations (2.8a–c), the following system of differential equations is obtained.

$$\begin{aligned} [(ikU - ED^2)\mathcal{D}^2 \tilde{w} + ik(\partial_y^2 U - \epsilon^{-2} \partial_z^2 U) \tilde{w} + 2ik\partial_y U \partial_y \tilde{w}] + \epsilon^{-2} \partial_z \tilde{\zeta} \\ - (2ik\epsilon^{-2})\partial_y U \partial_z \tilde{v} - (2ik\epsilon^{-2})\partial_{yz} U \tilde{v} - \epsilon^{-2} \mathcal{D}_h^2 \tilde{b} = -\sigma \mathcal{D}^2 \tilde{w}, \end{aligned} \quad (2.11a)$$

$$[-\partial_{yz} U \tilde{w} - \partial_z U \partial_y \tilde{w} + (\partial_y U - 1)\partial_z \tilde{w}] + [ikU - ED^2] \tilde{\zeta} - \partial_y^2 U \tilde{v} = -\sigma \tilde{\zeta}, \quad (2.11b)$$

$$\partial_z B \tilde{w} + \partial_y B \tilde{v} + [ikU - ED^2] \tilde{b} = -\sigma \tilde{b}, \quad (2.11c)$$

where $\mathcal{D}^4 = (\mathcal{D}^2)^2 = (\partial_y^2 + (1/\epsilon^2)\partial_z^2 - k^2)^2$ and $\mathcal{D}_h^2 = (\partial_y^2 - k^2)$. The eigenfunctions \tilde{u}, \tilde{v} are related to $\tilde{w}, \tilde{\zeta}$ by the relations from (2.9(a,b)),

$$-\mathcal{D}_h^2 \tilde{u} = ik\partial_z \tilde{w} + \partial_y \tilde{\zeta}, \quad (2.12a)$$

$$-\mathcal{D}_h^2 \tilde{v} = \partial_{yz} \tilde{w} - ik\tilde{\zeta}. \quad (2.12b)$$

We apply periodic boundary conditions in the y direction and free-slip, rigid lid, and zero buoyancy gradient boundary conditions in the z direction, i.e.,

$$\tilde{w} = \partial_{zz} \tilde{w} = \partial_z \tilde{\zeta} = \partial_z \tilde{b} = 0, \quad \text{at } z = 0, 1. \quad (2.13)$$

Equations (2.11a – c), with (2.12a – b) and (2.13) can be expressed as a standard generalized eigenvalue problem,

$$\mathbf{AX} = \sigma \mathbf{BX}, \quad (2.14)$$

where σ is the eigenvalue, $\mathbf{X} = [\tilde{w}, \tilde{\zeta}, \tilde{b}]^T$ is the eigenvector and the matrices \mathbf{A}, \mathbf{B} are the complex and real non-symmetric matrices, respectively. The elements of matrices \mathbf{A} and \mathbf{B} are shown in Appendix A. We solve the above eigenvalue problem following the procedure discussed in the next section.

2.2.2. Numerical method

To solve the eigenvalue problem (2.14), a spectral collocation method is used that utilizes Chebyshev differentiation in the z direction and Fourier differentiation in the y direction (Trefethen 2000). The generalized eigenvalue problem in (2.14) is solved using the FEAST algorithm, which is based on the complex contour integration method (Polizzi 2009). The benchmark of the eigensolver is presented in Appendix B.

To minimize the influence of periodic boundary conditions on the stability solution, the cross-front domain length is set to $3Ro^{-1/2}$, which ensures sufficient domain size (e.g., figure 6). The grid independent tests of the stability results are discussed in Appendix C. Unless otherwise stated, all results shown hereafter use $N_y = 240$ and $N_z = 32$, where N_y and N_z denote the number of points in the y and z directions, respectively.

2.2.3. Kinetic energy equation

The governing equation of the perturbation KE is given by

$$2\sigma \langle K \rangle_x + \underbrace{\langle \tilde{u}\tilde{v}^* - \tilde{u}^*\tilde{v} \rangle_x}_{\text{Coriolis}} = \underbrace{-\left\langle \tilde{u}^*\tilde{v} \frac{\partial U}{\partial y} \right\rangle_x}_{\text{HSP}} - \underbrace{\left\langle \tilde{u}^*\tilde{w} \frac{\partial U}{\partial z} \right\rangle_x}_{\text{VSP}} + \underbrace{\left\langle \tilde{w}^*\tilde{b} \right\rangle_x}_{\text{BFLUX}} + \underbrace{\left\langle \tilde{\nabla} \cdot (\tilde{u}^*\tilde{p}) \right\rangle_x}_{\text{PWORK}} + \underbrace{\left\langle E (\tilde{u}^*\nabla^2\tilde{u} + \tilde{v}^*\nabla^2\tilde{v} + \epsilon^2\tilde{w}^*\nabla^2\tilde{w}) \right\rangle_x}_{\text{DISP}}, \quad (2.15)$$

where $\langle \cdot \rangle_x$ denotes the x integral over one wavelength. The perturbation KE K is defined as $K = (\tilde{u}\tilde{u}^* + \tilde{v}\tilde{v}^* + \epsilon^2\tilde{w}\tilde{w}^*)/2$, with the superscript ‘star’ denoting a complex conjugate quantity. The term Coriolis in (2.15) is purely imaginary and thus does not contribute to the growth of the perturbation KE. The first two terms on the right-hand side of (2.15), horizontal shear production (HSP) and vertical shear production (VSP), are associated with the horizontal and vertical shear of the mean flow, respectively. A positive value of HSP (or VSP) describes the growth of the perturbation KE at the expense of the mean flow KE. The third term on the right-hand side of (2.15), the buoyancy flux (BFLUX), quantifies energy exchanges between the perturbation kinetic and potential energies. The pressure work (PWORK) term denotes the propagation of KE due to pressure perturbations and has a zero domain average. The dissipation term (DISP) for the unstable perturbation is negligible due to the small value of E in the stability analysis (not shown).

Throughout the manuscript, we define the domain integral (in y - z plane) of a quantity ϕ as

$$\langle \phi \rangle_{yz} = \int_{-1.5L_f}^{1.5L_f} \int_0^1 \phi dy dz, \quad (2.16)$$

and denote the volume integral of the quantity ϕ by $\langle \phi \rangle_{xyz}$.

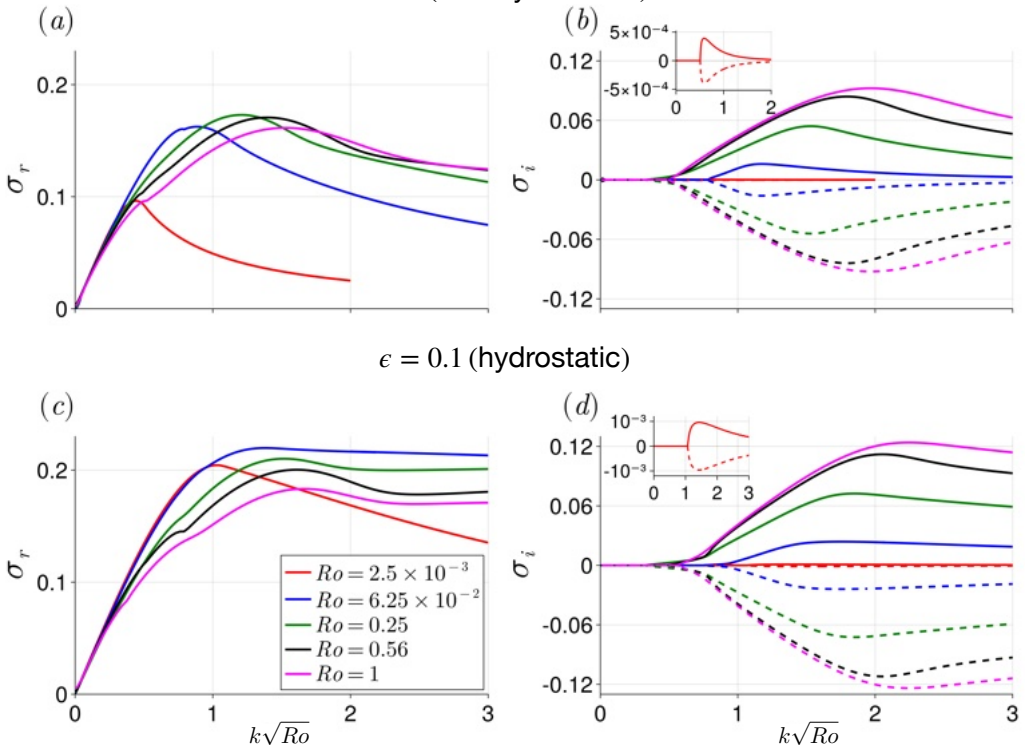


FIGURE 4. The nondimensional growth rate σ_r (panels (a, c)) and corresponding frequency σ_i (panels (b, d)) for different Ro values with $\epsilon = 1$ (top panels; non-hydrostatic regime) and $\epsilon = 0.1$ (bottom panels; hydrostatic regime). The insets in panels (b, d) zoom in on the frequency diagrams for the case of $Ro = 2.5 \times 10^{-3}$. Note that the wavenumber k is non-dimensionalized by the dimensional cross-frontal width $Ro^{-1/2}R$, the natural length scale of the adjusted front.

TABLE 1. The complex frequency σ^{ms} and corresponding wavenumber k^{ms} of the most unstable mode for different values of Ro . Note that k^{ms} is non-dimensionalized by the cross-frontal width $Ro^{-1/2}R$. Results are presented for two regimes, $\epsilon = 1$ and $\epsilon = 0.1$. Results from the QG linear stability analyses are also shown for four values of Ro . The zero frequency modes are the BCI modes.

Ro	$(Ro_\ell)_{\max}$	$\epsilon = 1$		$\epsilon = 0.1$		QG	
		$k^{\text{ms}}\sqrt{Ro}$	σ^{ms}	$k^{\text{ms}}\sqrt{Ro}$	σ^{ms}	$k^{\text{ms}}\sqrt{Ro}$	σ^{ms}
2.5×10^{-3}	2×10^{-3}	0.441	0.096	1.031	0.204	2.783	0.537
6.25×10^{-2}	0.05	0.887	$0.163 \pm 0.006i$	1.378	$0.219 \pm 0.021i$	2.753	0.525
0.25	0.25	1.211	$0.173 \pm 0.043i$	1.513	$0.210 \pm 0.063i$	2.556	0.429
0.56	0.76	1.394	$0.171 \pm 0.071i$	1.606	$0.201 \pm 0.097i$	2.347	0.328
1	3.23	1.538	$0.161 \pm 0.079i$	1.698	$0.188 \pm 0.106i$	—	—

3. Results

We examine the linear stability analyses of the basic state described by (2.3a – c) across a range of Rossby numbers (by varying $\beta \in [0.1, 2]$ with increments of 0.1), for two values of ϵ , $\epsilon = 1$ (non-hydrostatic) and $\epsilon = 0.1$ (hydrostatic). The nondimensional growth rate σ_r and the corresponding frequency σ_i as a function of the along-front wavenumber k for five different values of Ro are shown in figure 4. In contrast to the QG BCI described by Eady (1949) and the

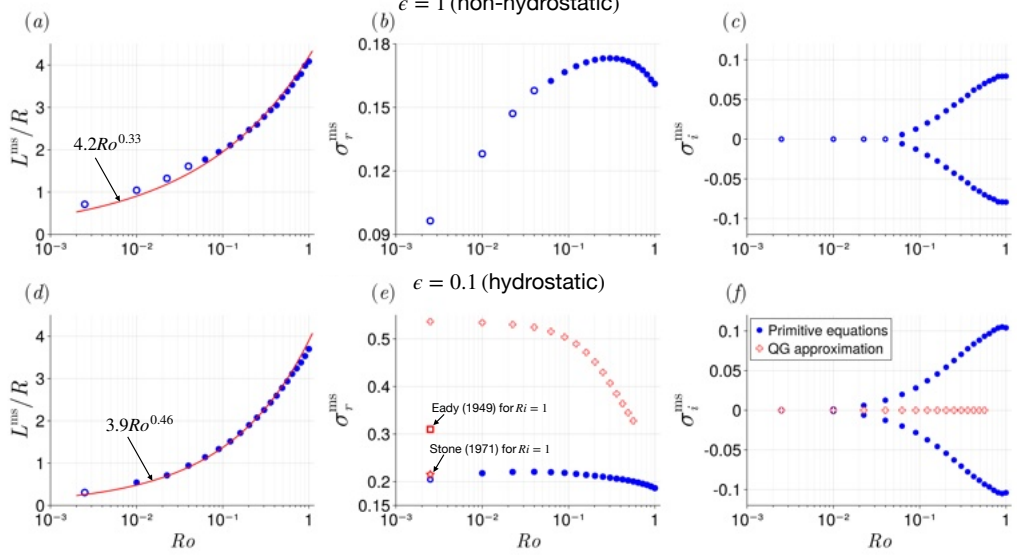


FIGURE 5. Panel (*a, d*) shows the non-dimensional wavelength of the most unstable mode $L_{\text{ms}}/R = (2\pi/k^{\text{ms}})$. The red lines in panels (*a, d*) represent the least-squares fits of L_{ms}/R as a function of Ro . The nondimensional growth rate of the most unstable mode, σ_r^{ms} (panels (*b, e*)), and the corresponding frequency, σ_i^{ms} (panels (*c, f*)), are shown for various Ro values. The top (bottom) panel shows for the non-hydrostatic (hydrostatic) regime. Open blue circles denote BCI modes, while filled circles represent ICL instability modes. Open crosses in panels (*c*) and (*d*) indicate growth rates and frequencies obtained from the QG stability analysis (Appendix D). For comparison, the growth rate of most unstable BCI mode of the S71 (red star) and Eady (red rectangle) solutions are shown for $Ri = 1$ and $\text{Ro} = 0$ (figure 13). The x -axes in all panels are shown on a logarithmic scale.

non-geostrophic BCI analysis of Stone (1966), the present analysis exhibits no short-wave cut-off in the perturbation growth rate (figures 4(*a, c*)). Notably, the frequency–wavenumber diagrams (figures 4(*b, d*)) reveal two distinct regimes – zero frequency and non-zero frequency (propagating modes).

The zero frequency regime corresponds to BCI, which can be interpreted as the phase locking of two counter-propagating Rossby waves situated in regions of opposing isopycnal PV gradients (Hoskins *et al.* 1985). In contrast, the non-zero frequency mode is identified as the inertia-critical layer (ICL) instability mode (see §3.1 for mode structure and discussion). The ICL instability mechanism is associated with a singularity at an ICL, where the Doppler-shifted frequency matches plus or minus the Coriolis frequency (Jones 1967). In nondimensional form, this condition is expressed as

$$k(U \pm \Delta U) - \sigma_i = \pm 1, \quad (3.1)$$

where $\Delta U = U_{\text{max}} - U_{\text{min}}$, with U_{max} and U_{min} denoting the global maximum and minimum values of U , respectively (e.g., figure 9(*a*)). The positive (negative) sign corresponds to perturbation frequency with positive (negative) σ_i in (3.1). Physically, the ICL acts as an absorber of inertia-gravity waves, facilitating the transfer of wave momentum to the mean flow (Jones 1967). The positive and negative frequency ICL instability modes have identical growth rates (figures 4(*a, c*)), with a positive (negative) frequency corresponding to a phase speed in the positive (negative) x -direction.

In the non-hydrostatic case, the growth rate, σ_r , decreases for large values of k for all Ro values (figure 4(*a*)). In contrast, in the hydrostatic case σ_r remains relatively constant for large k

values (with the exception of $Ro = 2.5 \times 10^{-3}$) indicating a broad range of unstable modes with comparable growth rates (figure 4(c)).

For the basic state considered by S71 the front has infinite width, whereas in the present analysis the cross-front width scales as $Ro^{-1/2}$. Consequently, at lower Ro value (i.e., $Ro = 2.5 \times 10^{-3}$, $Ri=1$; figure 3(b)), the growth rate of the most unstable BCI mode, σ_r^{ms} , approaches that reported by S71 (open blue circle for $Ro = 2.5 \times 10^{-3}$ and open red star in figure 5(c)), while the Eady solution has a larger growth rate (open red rectangle in figure 5(c)), likely due to the fact that the unstable mode is ageostrophic when $Ri = 1$. In contrast to the hydrostatic case, the most unstable mode in the non-hydrostatic regime remains of BCI type up to $Ro = 0.04$, with σ_r^{ms} increasing as Ro increases (figure 5(a)). This is a consequence of more APE in the frontal region at larger Ro (not shown). Non-hydrostatic effects also act to reduce the most unstable BCI wavenumber, k^{ms} ; for instance, at $Ro = 2.5 \times 10^{-3}$, k^{ms} decreases from approximately 20.61 to 8.83 as ϵ increases from 0.1 to 1 (see table 1 for comparison at $Ro = 2.5 \times 10^{-3}$).

As Ro increases, the dominant instability transitions to the ICL instability mode. The growth rate of the most unstable ICL mode is slightly higher in the hydrostatic case compared to the non-hydrostatic case (table 1). The growth rate of the most unstable ICL instability mode is largely independent of Ro in both hydrostatic and non-hydrostatic cases, while the wavenumber corresponding to the most unstable mode decreases with Ro in both cases. The wavenumber of the most unstable mode is consistently slightly larger in the hydrostatic case than in the non-hydrostatic case (table 1).

The QG stability analysis consistently overpredicts σ_r^{ms} (open plus symbols in figure 5(c)). The higher growth rate of the QG BCI mode at the low Ro is because the adjusted front exhibits strong horizontal variations in the stratification, while the QG analysis assumes that changes in the stratification are small.[†] The growth rate of the most unstable QG BCI mode decreases monotonically with increasing Ro , reflecting a suppression of BCI by horizontal shear. This is a well-documented effect, commonly referred to as the barotropic governor mechanism (James & Gray 1986; James 1987). Interestingly, when the most unstable QG BCI wavenumber is non-dimensionalized by the frontal width $Ro^{-1/2}R$, it remains largely insensitive to Ro (table 1). This implies that the cross-front length scale sets the wavelength of the most unstable QG BCI mode.

3.1. Mode structure

We can gain insight into the instability and the difference between the primitive equation and QG analysis by considering the spatial structure of the most unstable modes. We begin by analyzing the structure of the most unstable BCI mode with $Ro = 2.5 \times 10^{-3}$ at the bottom ($z = 0$) and top ($z = 1$) surfaces. Figures 6(a, b) show the most unstable QG BCI mode and figures 6(d, e) show the most unstable primitive equation mode in the hydrostatic case. The vertical relative vorticity is shown in panels (c) and (d) for reference. In both cases, the perturbation modes are confined in the cross-front direction, although the QG solution shows notably stronger cross-front localization than its primitive equations counterpart. The confinement is due to the fact that horizontal shear localizes the isopycnal PV gradient (horizontal gradient for QG dynamics), creating Rossby wave guides that confine the BCI mode (not shown; Hoskins *et al.* 1985). The BCI mode in the primitive equations exhibits a clear leftward tilt (figures 6(d, e)). Conversely, the corresponding QG BCI mode exhibits a weaker, rightward tilt (figures 6(a, b)). For $Ro = 0.25$, the rightward tilt in the QG BCI mode is more pronounced (figure 14), demonstrating the effect of horizontal shear on the perturbation mode structure.

For the positive-frequency ICL instability mode, the Rossby wave component is centered on the

[†] as expected, the low Rossby number QG BCI growth rate approaches that of Eady when using the same stratification value.

upper boundary of the domain, while the Doppler-shifted IGW is centered on the lower boundary (figures 6(*g, h*) and (*j, k*)). This vertical arrangement is reversed for the negative-frequency branch (not shown). The IGW mode is confined near the ICL ((3.1); dashed magenta line in figures 6(*g*) and (*j*)), whereas the Rossby wave is predominantly localized within the cyclonic vorticity region (figures 6(*h, i*) and (*k, l*)). The Rossby wave mode tilts against the horizontal shear, enabling it to extract energy from the horizontal shear of the frontal flow - consistent with the energetic interpretation discussed in the next section.

3.2. Energetics

The ICL instability modes consist of conjugate pairs of positive and negative frequency branches, each exhibiting identical growth rates (figure 5). From an energetic perspective, it is therefore natural to represent the perturbation solution as a linear superposition of these two modes. To facilitate comparison across different values of Ro , all perturbation quantities are scaled such that the volume-integrated perturbation KE equals 1.

As expected, the primary source of energy driving perturbation growth for the BCI modes is the buoyancy flux (BFLUX), with only minor contributions from the vertical shear production (VSP) and the horizontal shear production (HSP) (figures 7(*a, b*)). For the broad front and low Ro case ($Ro = 2.5 \times 10^{-3}$), $\langle BFLUX \rangle_{yz}$ closely matches the result of S71 (green circle and green star in figure 7(*b*)). The Eady solution tends to overpredict the buoyancy flux (green rectangle in figure 7(*b*)), again reflecting the fact that the unstable mode is no longer purely geostrophic when $Ri = 1$ (Stone 1971). In the non-hydrostatic regime, $\langle BFLUX \rangle_{yz}$ for the BCI mode increases with Ro (open green circles in figure 7(*a*)), consistent with the increase in APE (not shown). Furthermore, for the non-hydrostatic BCI modes ($Ro = 2.5 \times 10^{-3}$ to 0.04), $\langle VSP \rangle_{yz}$ remains significantly larger than $\langle HSP \rangle_{yz}$ (open blue and red circles in figure 7(*a*); see §3.2.1 for a discussion).

In contrast to the BCI modes, the ICL instability is driven by a combination of $\langle VSP \rangle_{yz}$, $\langle HSP \rangle_{yz}$, and $\langle BFLUX \rangle_{yz}$ (filled circles in figure 7(*a, b*)). For $Ro > 0.3$ the contribution from $\langle BFLUX \rangle_{yz}$ decreases and the contribution from $\langle HSP \rangle_{yz}$ increases in both hydrostatic and non-hydrostatic cases (filled green circles in figures 7(*a, b*)). In both cases, the sum of the horizontal and vertical shear production becomes comparable to the buoyancy flux when $Ro \sim \mathcal{O}(1)$.

In the QG solution, perturbation growth is primarily driven by the buoyancy flux ($\langle BFLUX^{QG} \rangle_{yz}$), which decreases monotonically with increasing Ro (green plus in Figure 7(*b*)), an effect attributed to the barotropic governor mechanism. The value of $\langle HSP^{QG} \rangle_{yz}$ is negative (red plus in Figure 7(*b*)), indicating a counter-gradient horizontal momentum flux. Its magnitude increases with Ro , consistent with the intensification of horizontal shear.

3.2.1. Spatial structure of energy exchange terms

Here, we examine the spatial structure of the energy exchange terms at two Rossby numbers - the BCI mode at $Ro = 2.5 \times 10^{-3}$ and the ICL instability mode at $Ro = 1$, both under hydrostatic conditions (figure 8). For the BCI mode, HSP is antisymmetric about $y = 0$ (figure 8(*a*)), a consequence of the negative correlation $\langle uv \rangle_x < 0$ (vector plots in figures 6(*b, c*)) and the antisymmetric structure of the horizontal shear $\partial_y U$ (figure 3(*a*)). As a result, the domain-integrated HSP is close to zero. This antisymmetric structure of HSP is also observed in the non-hydrostatic case (not shown), explaining why the domain-integrated HSP remains negligible for the BCI mode (figure 7(*a*)). In contrast, the VSP remains positive throughout the domain (figure 7(*b*)), resulting from the negative correlation $\langle uw \rangle_x < 0$ combined with the positive vertical shear $\partial_z U$ (not shown). The value of BFLUX is positive and strongly localized across the cross-front (figure 8(*c*)).

To further elucidate the energetics of the ICL instability mode and in particular the observed decrease in $\langle BFLUX \rangle_{yz}$ with increasing Ro (filled green circle in figures 7(*a, b*)), we examine the spatial structure of the energy exchange terms associated with the positive frequency branch

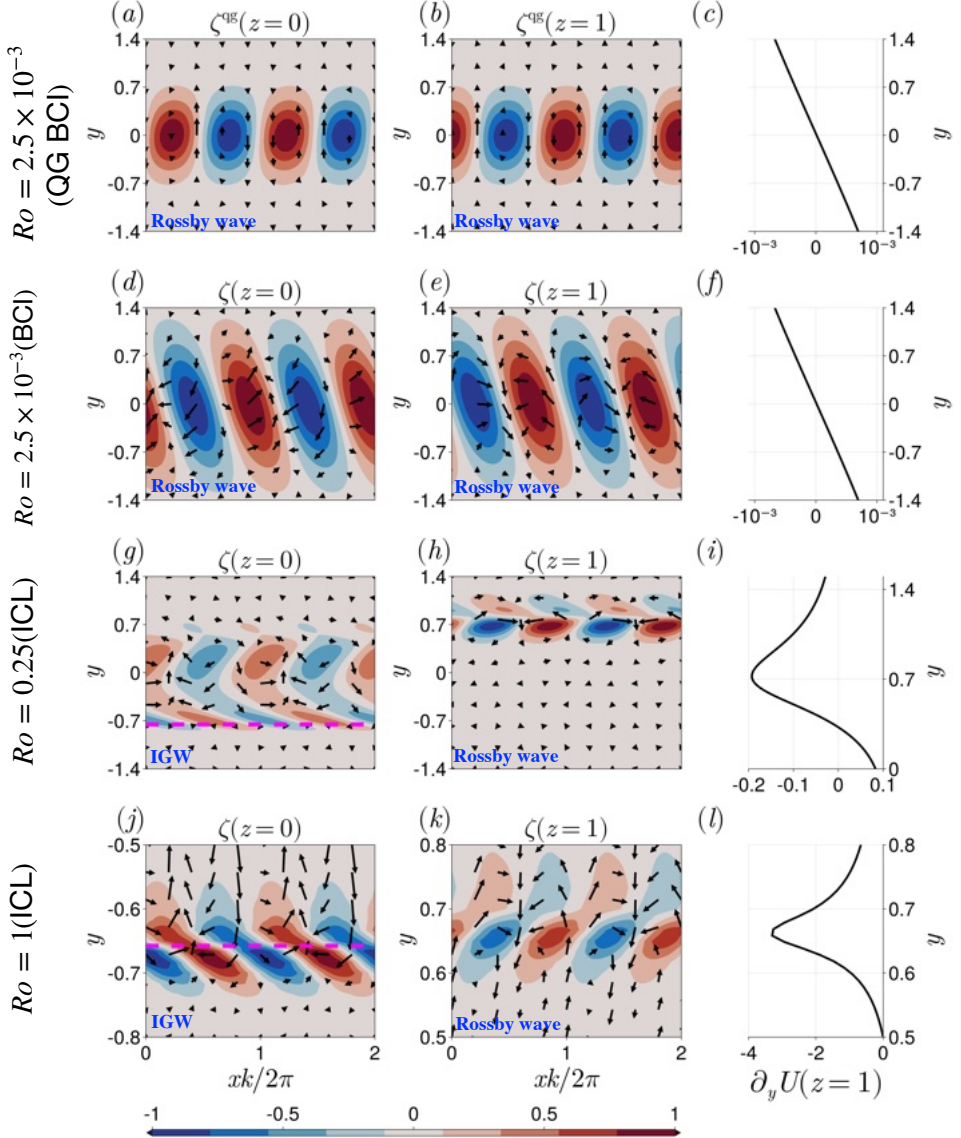


FIGURE 6. Comparison of perturbation vertical vorticity for the most unstable modes across different Ro values, computed based on the hydrostatic ($\epsilon = 0.1$) bi-global stability analysis. Panels (a, b) and (d, e) correspond to the BCI modes computed separately from the QG stability analysis (Appendix D) and from the primitive equation stability analysis, respectively, at $Ro = 2.5 \times 10^{-3}$. Panels (g, h) and (j, k) correspond to the ICL instability modes for the positive frequency branch, computed at $Ro = 0.25$ and $Ro = 1$, respectively. The left and middle columns show the vertical vorticity structures in the x - y plane at $z = 0$ and $z = 1$, respectively, while the right column (panels (c, f, i, l)) shows the corresponding horizontal shear $\partial_y U$ at $z = 1$. The velocity vectors normalized by their respective maximum amplitudes (embedded black arrows) show that the horizontal circulation is anticlockwise (clockwise) around regions of positive (negative) vertical vorticity for the Rossby wave modes. The dotted magenta lines in panels (g) and (h) show the ICL described by (3.1). The x -axis in all panels are scaled by the corresponding wavelength $2\pi/k$. Note that the y -axis limits in panels (j, k, l) differ from those of all other panels.

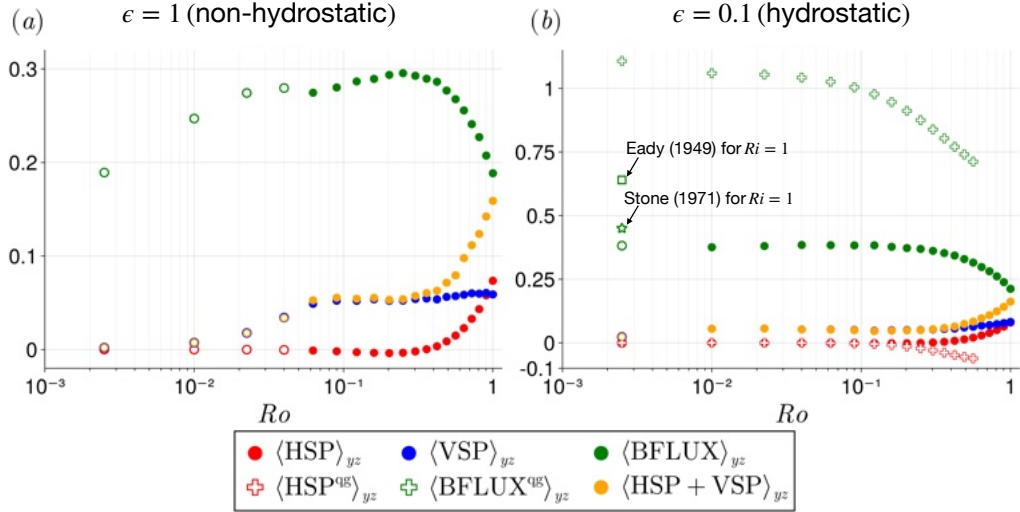


FIGURE 7. Domain integral (i.e., (2.16)) of the energy exchange terms (2.15) for the most unstable mode shown in figure 5 for the cases of (a) $\epsilon = 1$ and (b) $\epsilon = 0.1$. In panels (a, b), open (filled) symbol indicates BCI (ICL) mode. For the ICL modes, the energetics are computed from a linear superposition of the positive and negative frequency modes. For comparison, the corresponding QG energy terms (D 11) are shown in panel (b) (open red and green crosses). The open green star and rectangle symbols in panel (b) shows the S71 and Eady (1949) solutions, respectively for the case of $Ri = 1$ and $Ro = 0$. The x -axes in both panels are shown on a logarithmic scale.

(figures 8(d – f); the negative frequency branch exhibits a mirrored pattern). The positive HSP signal at the upper frontal region, where the vorticity is cyclonic (figure 8(d)), is associated with the Rossby wave (figure 6(k)). This arises as a result of the positive correlation between u and v in the upper part of the domain ($\langle uv \rangle_x > 0$; vector plots in figure 6(k) and figure 9(a)). At the lower frontal region HSP is positive near $z = 0$ and then changes sign from being positive to negative (figure 8(a)). This is because $\langle uv \rangle_x$ also changes sign from positive to negative with increasing z near the ICL region (figure 9(a)). This sign reversal of $\langle uv \rangle_x$ is an intrinsic property of an IGW that crosses the ICL (shown by dotted magenta line in figure 9(a); Maslowe 1986), and occurs because there is a $\pi/2$ phase shift in the IGW polarization relations between u and v . The magnitude of VSP for the ICL instability mode peaks at the top and bottom frontal regions (figure 8(b)), where the vertical shear is strong and positive (not shown). The negative (positive) VSP values near the top (bottom) frontal regions are associated with $\langle uw \rangle_x > 0$ ($\langle uw \rangle_x < 0$; figure 9(b)). BFLUX exhibits a sign change across the domain (figure 8(c)). Positive BFLUX values, associated with the Rossby wave in the upper domain, indicate the conversion of potential energy into kinetic energy. In contrast, negative BFLUX values are found in the lower frontal region and are related to the Doppler-shifted IGW.

The spatial structure of BFLUX can be analysed using the parcel method, a conceptual approach used to understand the mechanism of BCI (Thorpe *et al.* 1989). The flow is considered baroclinically unstable if a parcel is displaced adiabatically within the wedge of instability — defined as the region between the horizontal layer and the isopycnal slope. For instance, parcels labeled A and B experience instantaneous displacements that exceed the isopycnal slope, resulting in a negative BFLUX (see figure 10(a)). Conversely, parcels C and D undergo displacements that remain within the wedge of instability, leading to a positive BFLUX (see figure 10(b)). The magnitude of the negative BFLUX increases with increasing Ro , thereby explaining the observed decreases in $\langle BFLUX \rangle_{yz}$.

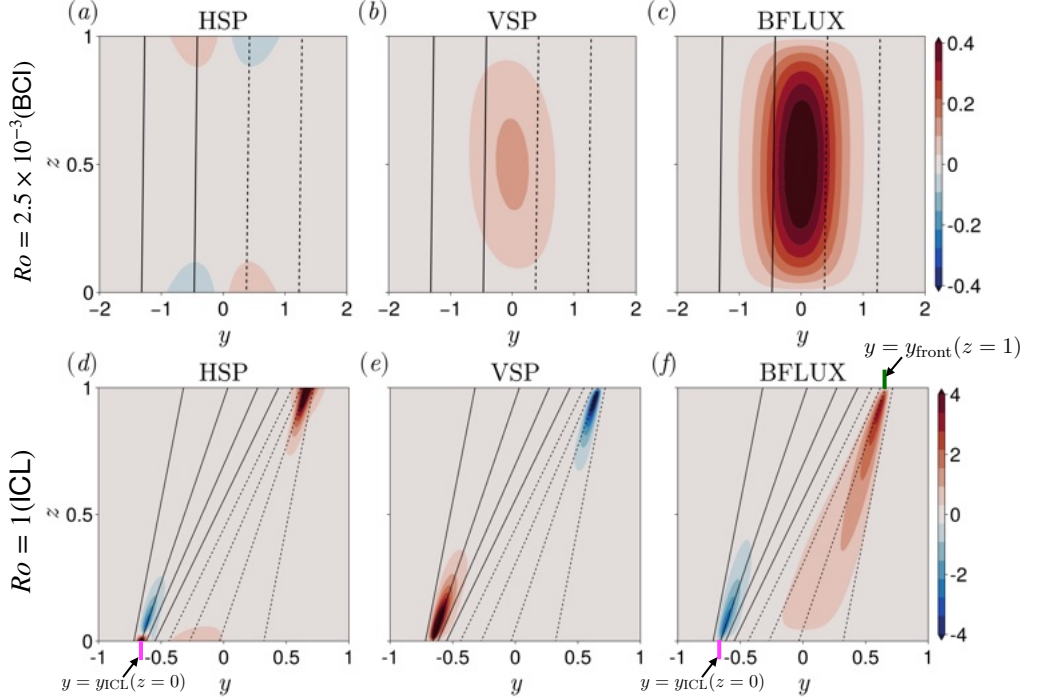


FIGURE 8. Color contour plots of energy exchange terms in the perturbation KE equation (2.15). Panels (a–c) show the BCI mode at $Ro = 2.5 \times 10^{-3}$, while panels (d–f) correspond to the ICL instability mode at $Ro = 1$, both under hydrostatic conditions. The black lines represent the adjusted isopycnals B , with contour intervals of 0.04 in panel (a–c) and 0.11 in panel (d–f). The solid (dashed) black lines indicate a positive (negative) values. The vertical magenta lines in panels (d) and (f) denote the location of the ICL – $y_{\text{ICL}} = -0.67$ at $z = 0$. The vertical green line in panel (c) marks the location of the maximum horizontal buoyancy gradient- $y_{\text{front}} = 0.65$ at $z = 1$.

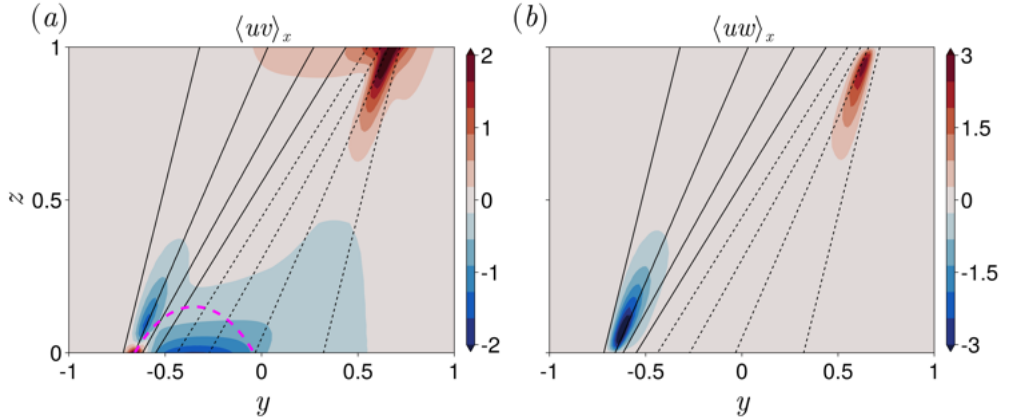


FIGURE 9. Color contour plots of the x -integrated correlation functions for the case $Ro = 1$ under hydrostatic conditions - (a) $\langle uv \rangle_x$ and (b) $\langle uw \rangle_x$. The black contours in both panels represent the adjusted isopycnal field B , plotted with a contour interval of 0.11; solid (dashed) lines indicate positive (negative) values. In panel (a), the dotted magenta line marks the location of the ICL as defined in (3.1).

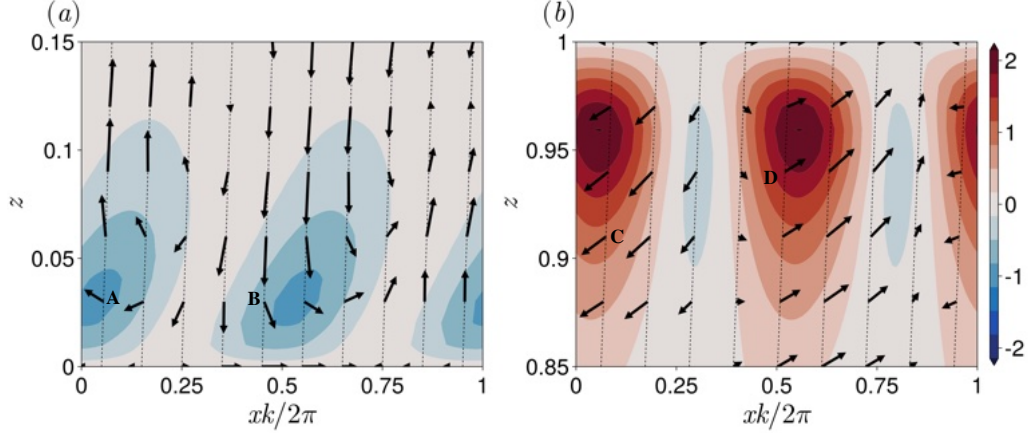


FIGURE 10. Vector plots illustrating parcel displacements in the y - and z -directions, represented by $\xi = Dv/Dt$ and $\eta = \epsilon Dw/Dt$, respectively, are shown for the case of $Ro = 1$ under hydrostatic conditions. Color contours display wb along the x -axis. Panels (a) and (b) correspond to cross-sections at $y = y_{ICL}$, $z = 0$, and $y = y_{front}$, $z = 0$, respectively (cf. figure 7(f)). Dashed lines in both panels indicate the angle of the adjusted isopycnals. The x -axis is normalized by the perturbation wavelength, $2\pi/k$. Only the lower and upper portions of the domain where the buoyancy flux is concentrated are shown in panels (a) and (b), respectively.

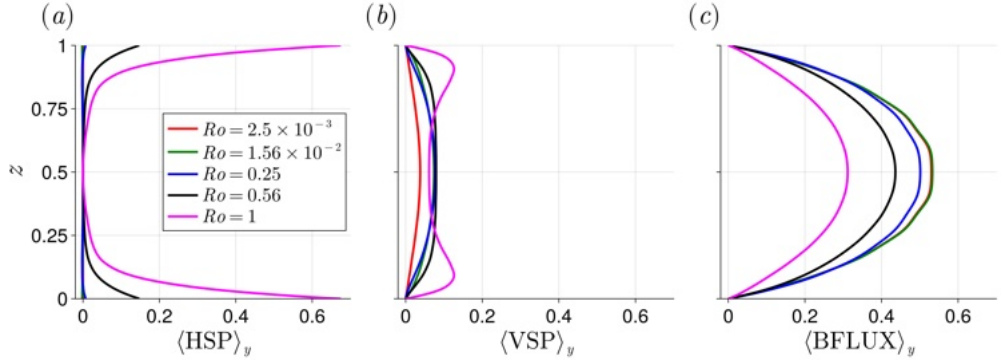


FIGURE 11. The vertical profiles of the energy exchange terms in (2.15) for different values of Ro in the hydrostatic case.

4. Discussion

4.1. Contrasting basic states: S71 and Ou84 in low- Ro limit

The remarkable agreement of the growth rates and buoyancy flux magnitudes between S71 and Ou84 for $Ro = 2.5 \times 10^{-3}$ (figures 5(e) and 7(b)) may give the false impression that the Ou basic state in the low- Ro broad-front limit (2.3a–c) approaches that of Stone (1971, (B 1a, b)), whereas they are, in fact, fundamentally different. For small Ro , the isopycnals in Ou84 adjust very slightly (figure 2(c)) and from (2.3(a)) we get

$$\eta \approx y - Ro^{1/2} \left(z - \frac{1}{2} \right). \quad (4.1)$$

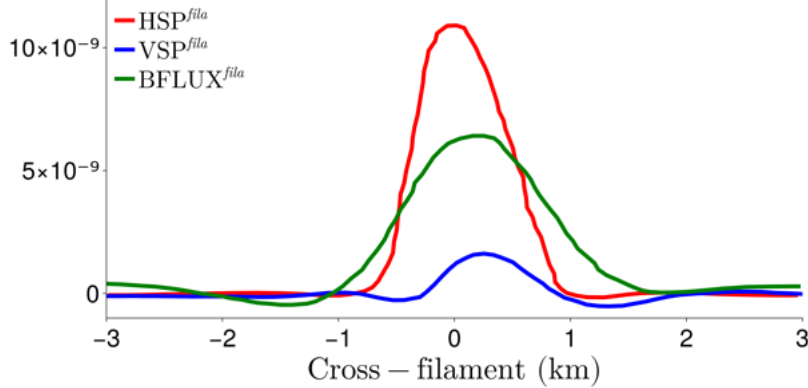


FIGURE 12. Perturbation KE analysis of a frontal instability in a high-resolution (150m horizontal grid spacing) realistic simulation in the Mississippi River plume system, adapted from Wang *et al.* (2021). Mean flow quantities are defined as along-front averages, while perturbation quantities represent deviations from this mean. Based on these decompositions, the exchange terms are - $HSP^{fila} = -\overline{u'^2}\partial\bar{u}/\partial x - \overline{v'^2}\partial\bar{v}/\partial y - \overline{u'v'}(\partial\bar{u}/\partial y + \partial\bar{v}/\partial x)$, $VSP^{fila} = -\overline{u'w'}\partial\bar{u}/\partial z - \overline{v'w'}\partial\bar{v}/\partial z$, and $BFLUX^{fila} = \overline{w'b'}$, which are averaged over the top 10m. The physical interpretation of these terms remains the same as discussed in (2.15). The overbar denotes an along-front mean, and the prime denotes a perturbation quantity.

With $Ro^{1/2}\eta \ll 1$, $\tanh(\beta\eta) \approx \beta\eta$ and (2.4), (2.3c) reduce to

$$B(y, z) \approx -Ro^{1/2}y + Ro\left(z - \frac{1}{2}\right), \quad (4.2a)$$

$$U(y, z) \approx Ro^{1/2}\left(z - \frac{1}{2}\right), \quad (4.2b)$$

which satisfies the thermal-wind relation ($\partial_z U = -\partial_y B$). Interestingly, the local Richardson number of the basic state $Ri_\ell = \partial_z B / (\partial_z U)^2 \sim 1$ because $\partial_z B$ and $(\partial_z U)^2$ both scale with Ro (consistent with figure 3(b)). Thermal wind balance is also satisfied for the Stone (1971) basic state (B 1a, b), but $Ri \sim 1$ only occurs when $\partial_z B \sim \partial_z U \sim 1$.

4.2. Length scales and energetics

The dimensional wavelength of the most unstable mode, L^{ms} , increases with Ro under both hydrostatic and non-hydrostatic cases (figures 5(a, d), $L^{ms}/R \approx 4.2Ro^{1/3}, 3.9Ro^{1/2}$ for non-hydrostatic and hydrostatic cases, respectively), emphasizing the influence of horizontal shear on the instability characteristics. For $Ro = 1$, $L^{ms} \approx 4R$. Using representative oceanic ML parameters in the mid-latitude during winter (e.g., $H = 100$ m, $f = 10^{-4}$ s $^{-1}$ and $N = 10f$ s $^{-1}$) yields a deformation radius $R = 1$ km and $L^{ms} \approx 4$ km, consistent with the length scale of submesoscale frontal instabilities (Wang *et al.* 2021).

As expected for the BCI regime, the dominant source of perturbation energy is the buoyancy flux (open green symbol in figure 7). As Ro increases, the vertical and horizontal shear production grow and their sum becomes comparable to the buoyancy flux when $Ro = 1$ (orange and green symbols in figure 7). For larger Ro , we anticipate that the shear production terms will continue to grow while the buoyancy flux will continue to weaken, making the shear production terms the dominant source of perturbation energy for $Ro \gg 1$. We note in passing that in the oceanic ML, the vertical shear is likely weaker than in our stability analysis due to the continuous vertical mixing of momentum, and so the stability analysis may overestimate the vertical shear production.

Dong *et al.* (2020) estimated that the typical length scale of the most unstable MLI mode is

about 6 km at mid-latitudes, implying that a horizontal grid spacing of order 1 km is needed to resolve it in oceanic regional models. At this resolution, the local Rossby number is typically $\mathcal{O}(1)$ (Capet *et al.* 2008a; Barkan *et al.* 2017). Therefore, the shear production terms (mainly HSP) are expected to significantly affect MLI characteristics at this scale.

Standard efforts to parametrize the effects of MLI in coarse-resolution climate models (e.g., Fox-Kemper *et al.* 2008; Bodner *et al.* 2023) focus on the restratification effects associated with the buoyancy flux and do not include the horizontal or vertical shear production. Our work suggests that when $Ro \geq 1$, existing parametrizations may miss critical energy pathways that are essential for adequately representing submesoscale physics in global ocean circulation models.

4.3. Frontal arrest

In realistic oceanic settings, frontogenesis sharpens horizontal buoyancy gradients and horizontal shear at a super-exponential rate (Barkan *et al.* 2019), a process tending towards a finite-time singularity in the inviscid limit. Ultimately, an instability mechanism may arrest this sharpening before the singularity is reached (e.g., Sullivan & McWilliams 2024). At the arrested stage, fronts typically exhibit $Ro \gg 1$, and the vorticity field becomes strongly asymmetric, characterized by intense, spatially localized cyclonic vorticity with broader and weaker anticyclonic counterparts.

Although the basic state in our solution does not fully attain such high Rossby numbers, it captures these salient features already at $Ro = 1$ (figure 3(c)). At this Rossby number, the horizontal shear production is large and strongly confined near the upper and lower frontal flanks, while the vertical shear production is only marginally stronger than for lower Rossby number results (figures 11(a, b)). In contrast, the buoyancy flux weakens with increasing Ro and remains symmetric with respect to the domain mid-depth. At these frontal regions, the perturbation KE budget is dominated by the horizontal shear production and buoyancy flux, with the vertical shear production contributing marginally (typical values averaged over regions exceeding the 80th percentile of horizontal buoyancy gradients are HSP = 0.15, VSP = 0.05, and BFLUX = 0.13 for the horizontal shear production, vertical shear production, and buoyancy flux, respectively). This energetic signature closely matches previously reported results from a submesoscale-resolving realistic-ocean simulation by Wang *et al.* (2021), where the frontal arrest was driven predominantly by the horizontal shear production and buoyancy flux, with the vertical shear production remaining slightly positive (figure 12). A similar pattern emerges in the large-eddy simulation study of arrested filament evolution by Sullivan & McWilliams (2018), who linked frontal arrest to horizontal shear instability.

5. Summary

In this study, we perform a bi-global linear stability analysis of geostrophically adjusted 2D fronts with zero PV, archetypical of weakly stratified oceanic mixed layers. The frontal configuration follows the analytical solution developed by Ou (1984), allowing for a systematic examination of frontal stability characteristics across a broad range of Rossby numbers.

For low Rossby numbers, the most unstable mode resembles that of classical baroclinic instability. Namely, its growth rate agrees closely with the prediction of Stone (1971), and the source of perturbation growth comes solely from the buoyancy flux. Despite these similarities, the low Rossby number Ou (1984) basic state describes a different dynamical regime than that investigated by Stone (1971).

As the Rossby number increases, the dominant instability transitions to an inertia-critical layer (ICL) instability mode, with conjugate pairs of positive and negative frequencies exhibiting equal growth rates. This instability results from a resonance between a Rossby wave supported by the isopycnal potential vorticity gradient and an inertia-gravity wave.

At the order-one Rossby number regime, the buoyancy flux magnitude is comparable to the

sum of vertical and horizontal shear production, with the latter dominating near the region where the adjusted front is the strongest. In this regime, the instability agrees with the frontal arrest mechanism discussed by Sullivan & McWilliams (2018), whereby frontal intensification is halted by horizontal shear instability.

Mixed-layer instability (MLI) is traditionally viewed as a purely baroclinic process that restratifies the ML by releasing the available potential energy stored in horizontal buoyancy gradients (Boccaletti *et al.* 2007). The present stability analysis suggests that MLI can exhibit features of ICL instability, with a comparable growth rate to the mixed layer baroclinic instability but exhibiting both baroclinic and barotropic characteristics. This can have important implications for submesoscale parametrizations in ocean models.

Existing MLI parameterization schemes that are based on $Ro \ll 1$, $Ri \sim \mathcal{O}(1)$ baroclinic instability theory may fail to capture key energetic processes in realistic, ageostrophic fronts. In particular, horizontal shear production, which is significant in the $Ro \sim \mathcal{O}(1)$ regime, is completely ignored in mixed layer eddy parameterizations (e.g., Fox-Kemper *et al.* 2008). This highlights the need for revised parametrization frameworks that incorporate both baroclinic and barotropic instability mechanisms, particularly under conditions of strong frontal intensification, to more accurately represent upper-ocean restratification and kinetic energy dissipation.

Acknowledgements

SK and RB are supported by ISF grant 2054/23 and by the European Union (ERC, 401 ML Transport, 101163887). Views and opinions expressed are, however, those of the author(s) only and do not necessarily reflect those of the European Union or the European Research Council. Neither the European Union nor the granting authority can be held responsible for them.

Declaration of Interests

The authors report no conflicts of interest.

Data availability statement

The linear stability code used in this study is available at https://github.com/subhk/Frontal_Stability.

Appendix A. Matrices of the generalized eigenvalue problem

The elements of \mathbf{A} and \mathbf{B} of (2.14) are given by

$$\mathbf{A} = \begin{pmatrix} a_{11} & a_{12} & a_{13} \\ a_{21} & a_{22} & 0 \\ a_{31} & (ik\partial_y BI)H & ikUI - ED^2 \end{pmatrix}, \quad \mathbf{B} = \begin{pmatrix} -D^2 & 0 & 0 \\ 0 & -I & 0 \\ 0 & 0 & -I \end{pmatrix}, \quad (\text{B1b, c})$$

where

$$\begin{aligned} a_{11} &= (ikUI)D^2 - ED^4 + ik\left(\partial_y^2 U - \frac{1}{\epsilon^2}\partial_z^2 U\right)I + (2ik\partial_y UI)(D_y \otimes I_z) \\ &\quad + \left(\frac{2}{\epsilon^2}ik\partial_y UI\right)H(D_y \otimes D_z^2) + \left(\frac{2}{\epsilon^2}ik\partial_{yz} UI\right)H(D_y \otimes D_z), \end{aligned} \quad (\text{A 2a})$$

$$a_{12} = \frac{1}{\epsilon^2}I_y \otimes D_z + \left(\frac{2}{\epsilon^2}k^2\partial_y UI\right)H(I_y \otimes D_z) + \left(\frac{2}{\epsilon^2}k^2\partial_{yz} UI\right)H, \quad (\text{A 2b})$$

$$a_{13} = -\frac{1}{\epsilon^2}(D_y^2 \otimes I_z - k^2 I) \quad (\text{A 2c})$$

$$\begin{aligned} a_{21} &= -\partial_{yz} UI - \partial_z UI(D_y \otimes I_z) + \partial_y UI(I_y \otimes D_z) - (I_y \otimes D_z) \\ &\quad + (\partial_y^2 UI)H(D_y \otimes D_z), \end{aligned} \quad (\text{A 2d})$$

$$a_{22} = ikUI - ED^2 - (ik\partial_y^2 UI)H, \quad (\text{A 2e})$$

$$a_{31} = \partial_z BI - (\partial_y BI)H(D_y \otimes D_z), \quad (\text{A 2f})$$

where \otimes is the Kronecker product. I_y and I_z are identity matrices of size $(N_y \times N_y)$ and $(N_z \times N_z)$ respectively, and $I = I_y \otimes I_z$. The differential operator matrices are given by

$$D^2 = \frac{1}{\epsilon^2}I_y \otimes D_z^2 + D_y^2 \otimes I_z - k^2 I, \quad (\text{A 3a})$$

$$D^4 = \frac{1}{\epsilon^4}I_y \otimes D_z^4 + D_y^4 \otimes I_z + k^4 I - 2k^2 D_y^2 \otimes I_z - \frac{2k^2}{\epsilon^2}I_y \otimes D_z^2 + \frac{2}{\epsilon^2}D_y^2 \otimes D_z^2, \quad (\text{A 3b})$$

$$H = (D_y^2 \otimes I_z - k^2 I)^{-1}, \quad (\text{A 3c})$$

where H describes the inverse of the horizontal Laplacian operator.

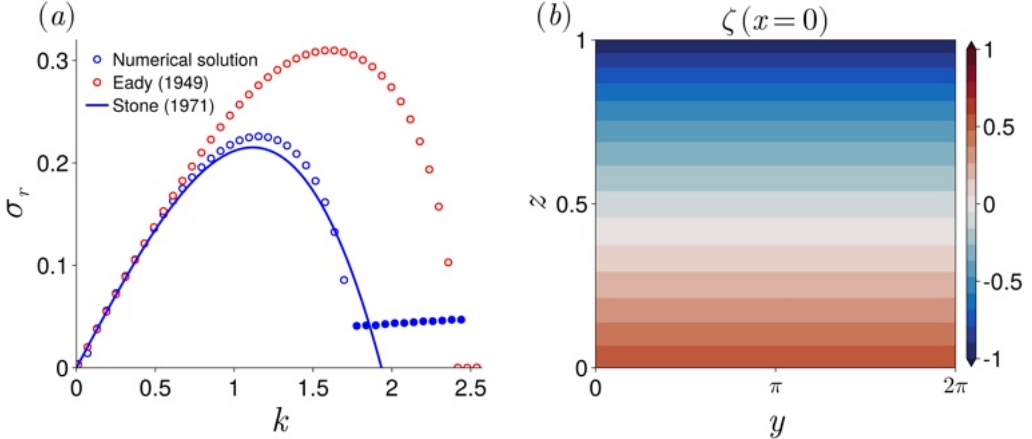


FIGURE 13. (a) Comparison of numerically obtained growth rate σ_r (blue circle) with the analytical solution of Stone (1971, blue line) given by (B 2), for $\epsilon = 0.1$ and $Ri = 1$. Also shown is the growth rate obtained from the QG approximation (Eady 1949, open red circles; see Appendix D). Open blue circle shows the BCI modes, while filled blue circle represent ICL modes. (b) The vertical vorticity ζ for the most unstable BCI mode ($k = 1.16$) from the numerical solution. The domain sizes are $y \in [0, 2\pi]$ and $z \in [0, 1]$, respectively, and the solutions are obtained using a grid resolution of $N_y = 120$ and $N_z = 24$.

Appendix B. Benchmark of the stability code

The linear stability code used in this study is benchmarked against the asymptotic solution for BCI by Stone (1971). The nondimensional form of the basic state is

$$U(y, z) = z - \frac{1}{2}, \quad (\text{B } 1a)$$

$$B(y, z) = Riz - y. \quad (\text{B } 1b)$$

Stone (1966) derived an analytical approximation for the growth rate as a function of along-front wavenumber k by expanding the eigenvalue problem for small k and $l = 0$, where l is the wavenumber in the cross-front (y) direction. The approximate growth rate of the most unstable BCI mode, σ_r^{Stone} , is given by

$$\sigma_r^{\text{Stone}} \approx \frac{1}{2\sqrt{3}} \left[k - \frac{2k^3}{15} \left(1 + Ri + \frac{5k^2\epsilon^2}{42} \right) \right], \quad (\text{B } 2)$$

where $\epsilon = H/R$. Stone's asymptotic solution (B 2) with $Ri = 1$ provides a good approximation to the numerical results for $k \lesssim 2$ (open blue circles in figure 13(a)). In contrast, the solution of Eady (1949) overestimates the growth rate in this regime. The discrepancy arises because, at $Ri = 1$, ageostrophic effects become non-negligible and are not captured by the QG framework. Unlike Stone's solution, the numerical results do not exhibit a short-wave cutoff for instability. At $k \gtrsim 2$, the perturbation modes have relatively smaller growth rates (filled blue circles in figure 13(a); see also figure 2 of Stone 1970). This branch of instability arises from a resonant interaction between a Rossby wave and a Doppler-shifted internal gravity wave (IGW) (Nakamura 1988). Nevertheless, the structure of the most unstable BCI mode remains invariant in the cross-front (y) direction, consistent with the theoretical prediction of (Stone 1966, figure 13(b)).

Appendix C. Grid independent test of the stability results

Grid resolution convergence tests for the most unstable mode were conducted for two extreme values of Ro - $Ro = 2.5 \times 10^{-3}$ and $Ro = 1$. The growth rate of the most unstable mode

TABLE 2. Grid convergence tests for the linear stability analysis in the hydrostatic regime were performed for the most unstable mode. Results are shown for two cases - $Ro = 2.5 \times 10^{-3}$ at $k = 20.614$, and $Ro = 1$ at $k = 1.698$ (figure 4). N_y and N_z denote number of grid points in the y and z directions, respectively.

$(N_y \times N_z)$	$\sigma(Ro = 2.5 \times 10^{-3})$	$\sigma(Ro = 1)$
(24×120)	0.2043	$0.1872 \pm 0.1053i$
(24×240)	0.2043	$0.1881 \pm 0.1061i$
(32×240)	0.2043	$0.1881 \pm 0.1061i$

converges at $N_y = 240$ and $N_z = 32$ (table 2). Accordingly, all results presented in this paper are based on $N_y = 240$ and $N_z = 32$.

Appendix D. Formulation of the 2D QG stability analysis

In this section, we outline the formulation of the 2D QG stability problem. The non-dimensional form of the linearized version of the QG PV perturbation equation under the f -plane approximation can be expressed as (Pedlosky 2013),

$$\frac{\partial q^{qg}}{\partial t} + U \frac{\partial q^{qg}}{\partial x} + \frac{\partial \psi}{\partial x} \frac{\partial Q^{qg}}{\partial y} = E \nabla_h^2 q^{qg}, \quad \text{for } 0 < z < 1, \quad (\text{D } 1)$$

where q^{qg} is the perturbation QG PV, and it is defined as

$$q^{qg} = \nabla_h^2 \psi^{qg} + \frac{\partial}{\partial z} \left(\frac{1}{N^2} \frac{\partial \psi^{qg}}{\partial z} \right), \quad (\text{D } 2)$$

where N^2 describes the stratification profile averaged over the frontal zone, and it is defined as

$$N^2(z) = \frac{1}{L_f} \int_{-L_f/2}^{L_f/2} \partial_z B dy, \quad (\text{D } 3)$$

where $L_f = Ro^{-1/2}$ is the cross-frontal width. The variable ψ^{qg} describes the QG perturbation streamfunction with $u^{qg} = -\partial_y \psi^{qg}$ and $v^{qg} = \partial_x \psi^{qg}$. The variable Q^{qg} describes the QG PV of the basic state, which is defined as (Pedlosky 2013)

$$Q^{qg} = -\frac{\partial U}{\partial y} + \frac{\partial}{\partial z} \left(\frac{B}{N^2} \right), \quad (\text{D } 4)$$

and the cross-front gradient of Q^{qg} is defined as

$$\frac{\partial Q^{qg}}{\partial y} = -\frac{\partial^2 U}{\partial y^2} - \frac{\partial}{\partial z} \left(\frac{\partial_z U}{N^2} \right). \quad (\text{D } 5)$$

The linearized perturbation buoyancy equation at the top and the bottom boundary is

$$\frac{\partial b^{qg}}{\partial t} + U \frac{\partial b^{qg}}{\partial x} + \frac{\partial \psi^{qg}}{\partial x} \frac{\partial B}{\partial y} = 0, \quad \text{at } z = 0 \text{ and } 1, \quad (\text{D } 6)$$

where $b^{qg} = \partial_z \psi^{qg}$. Next, we seek normal-mode solutions for ψ^{qg} and q^{qg} in the form of

$$[\psi^{qg}, q^{qg}] = \Re([\tilde{\psi}^{qg}, \tilde{q}^{qg}]) (y, z) e^{ikx - \sigma t}, \quad (\text{D } 7)$$

where $\tilde{\psi}^{\text{qg}}$, \tilde{q}^{qg} are the eigenfunctions of ψ^{qg} and q^{qg} , respectively. Using (D 7), (D 1), and (D 2), (D 6) can be expressed in terms of streamfunction ψ^{qg} ,

$$[(\sigma + ikU) - E]\mathcal{L}\tilde{\psi}^{\text{qg}} + ik\partial_y Q^{\text{qg}}\tilde{\psi}^{\text{qg}} = 0, \quad \text{for } 0 < z < 1, \quad (\text{D 8a})$$

$$(\sigma + ikU_-)\partial_z\tilde{\psi}_-^{\text{qg}} + ik\partial_y B_-\tilde{\psi}_-^{\text{qg}} = 0, \quad \text{at } z = 0, \quad (\text{D 8b})$$

$$(\sigma + ikU_+)\partial_z\tilde{\psi}_+^{\text{qg}} + ik\partial_y B_+\tilde{\psi}_+^{\text{qg}} = 0, \quad \text{at } z = 1, \quad (\text{D 8c})$$

where \mathcal{L} is a linear operator defined as

$$\mathcal{L} \equiv \mathcal{D}_h^2 + \frac{\partial}{\partial z} \left(\frac{1}{N^2} \frac{\partial}{\partial z} \right), \quad (\text{D 9})$$

and $\mathcal{D}_h^2 = (\partial_y^2 - k^2)$. The subscripts $-$, $+$ in (D 8b, c) denote the values of the fields at $z = 0$ and $z = 1$, respectively. The above set of equations can be cast into a generalized eigenvalue problem similar to (2.14). We followed similar numerical techniques as discussed in §2.2.2 to solve the eigenvalue problem.

We benchmarked the QG stability solver against the analytical solution of the Eady problem, using the basic state given by (B 1) in Appendix B 1. Following the procedure outlined by Vallis (2017), we derived the analytical expression for the growth rate,

$$\sigma_r^{\text{Eady}} = \frac{1}{\sqrt{Ri}} \left[\left(\coth \frac{\mu}{2} - \frac{\mu}{2} \right) \left(\frac{\mu}{2} - \tanh \frac{\mu}{2} \right) \right]^{1/2}, \quad (\text{D 10})$$

where $\mu = k\sqrt{Ri}$. The wavenumber of the most unstable mode is given by $k_m = 1.61/\sqrt{Ri}$. For $Ri = 1$, the numerically obtained growth rate at $k_m = 1.61$, $\sigma_r \approx 0.31$, which matches with the theoretical prediction (D 10).

D.1. Structure of mode

The Rossby wave mode is predominantly localized within the region of anticyclonic vorticity (figures 14(a, c)) and exhibits a rightward tilt (figures 14(a, b)). This spatial structure is indicative of the generation of a counter-gradient horizontal momentum flux, with $\langle u^{\text{qg}} v^{\text{qg}} \rangle_x > 0$, which tends to reinforce the background horizontal shear (figure 14(c)). As a result, $\langle \text{HSP}^{\text{qg}} \rangle_x$ becomes negative, reflecting a net transfer of energy from the perturbation field to the frontal flow (red crosses in figure 7b).

D.2. QG energetics

In the QG formalism, the evolution of the perturbation KE can be written as (Pedlosky 2013)

$$2\sigma\langle K^{\text{qg}} \rangle_x = \underbrace{\langle -\tilde{u}^{\text{qg}*} \tilde{v}^{\text{qg}} \frac{\partial U}{\partial y} \rangle_x}_{\text{HSP}^{\text{qg}}} + \underbrace{\langle \tilde{w}^{\text{qg}*} \tilde{b}^{\text{qg}} \rangle_x}_{\text{BFLUX}^{\text{qg}}} + \underbrace{\langle \tilde{\nabla} \cdot (\tilde{u}^* \tilde{p}) \rangle_x}_{\text{PWORK}^{\text{qg}}} \\ + \underbrace{\langle E \left(\tilde{u}^{\text{qg}*} \nabla_h^2 \tilde{u}^{\text{qg}} + \tilde{v}^{\text{qg}*} \nabla_h^2 \tilde{v}^{\text{qg}} \right) \rangle_x}_{\text{DISP}^{\text{qg}}}, \quad (\text{D 11})$$

where K^{qg} is the QG perturbation KE, defined as $K^{\text{qg}} = (\tilde{u}^{\text{qg}} \tilde{u}^{\text{qg}*} + \tilde{v}^{\text{qg}} \tilde{v}^{\text{qg}*})/2$. The physical interpretations of horizontal shear production (HSP^{qg}), buoyancy flux (BFLUX^{qg}), and pressure work (PWORK^{qg}) in the QG formalism are identical to those discussed in (2.15). The dissipation term (DISP^{qg}) is negligible for the unstable perturbations due to the small value of E used in the stability analysis (not shown). The variable w^{qg} denotes the vertical velocity in the QG approximation and is obtained by solving the QG ω -equation (Hoskins *et al.* 1978, see next section).

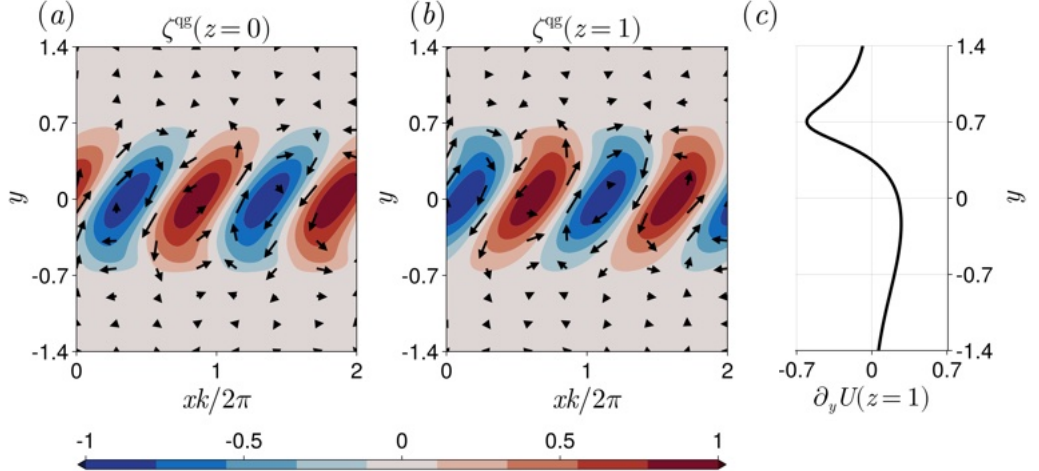


FIGURE 14. Structure of QG vertical vorticity $\zeta^{\text{qg}} (= \nabla_h^2 \psi^{\text{qg}})$ (a) at $z = 0$ and (b) at $z = 1$ for the case of $Ro = 0.56$ (corresponds to $\beta = 1.5$), with superimposed horizontal velocity vector $(u^{\text{qg}}, v^{\text{qg}})$ shown by the black arrows. The horizontal circulation in panels (a, b) is clockwise (anticlockwise) around the negative (positive) vorticity region. The velocity vectors in panels (a) and (b) are normalized by their respective maximum velocity amplitudes. The x -axis in panels (b, c) are normalized the wavelength $2\pi/k$. Panel (d) shows the horizontal shear $\partial_y U$ at $z = 1$.

D.3. Calculating vertical velocity

The nondimensional form of the QG ω equation can be expressed as (Hoskins *et al.* 1978)

$$N^2 \nabla_h^2 w^{\text{qg}} + \frac{\partial^2 w^{\text{qg}}}{\partial z^2} = 2 \nabla_h \cdot \mathcal{Q}, \quad (\text{D } 12)$$

where \mathcal{Q} is defined as

$$\mathcal{Q} = - \left(\frac{\partial v^{\text{qg}}}{\partial x} \frac{\partial B}{\partial y}, \frac{\partial U}{\partial y} \frac{\partial b^{\text{qg}}}{\partial y} + \frac{\partial v^{\text{qg}}}{\partial y} \frac{\partial B}{\partial y} \right). \quad (\text{D } 13)$$

Equation (D 12) is solved subject to rigid-lid boundary conditions at $z = 0$ and $z = 1$, and periodic boundary conditions in the cross-front (y) direction.

REFERENCES

- BALWADA, DHRUV, XIE, JIN-HAN, MARINO, RAFFAELE & FERACO, FABIO 2022 Direct observational evidence of an oceanic dual kinetic energy cascade and its seasonality. *Science Advances* **8** (41), eabq2566.
- BARKAN, ROY, McWILLIAMS, JAMES C, SHCHEPETKIN, ALEXANDER F, MOLEMAKER, M JEROEN, RENAULT, LIONEL, BRACCO, ANNALISA & CHOI, JUN 2017 Submesoscale dynamics in the northern gulf of mexico. part i: Regional and seasonal characterization and the role of river outflow. *Journal of Physical Oceanography* **47** (9), 2325–2346.
- BARKAN, ROY, MOLEMAKER, M JEROEN, SRINIVASAN, KAUSHIK, McWILLIAMS, JAMES C & D'ASARO, ERIC A 2019 The role of horizontal divergence in submesoscale frontogenesis. *Journal of Physical Oceanography* **49** (6), 1593–1618.
- BARTH, JOHN A 1994 Short-wave length instabilities on coastal jets and fronts. *Journal of Geophysical Research: Oceans* **99** (C8), 16095–16115.
- BOCCALETI, GIULIO, FERRARI, RAFFAELE & FOX-KEMPER, BAYLOR 2007 Mixed layer instabilities and restratification. *Journal of Physical Oceanography* **37** (9), 2228–2250.
- BODNER, ABIGAIL S, FOX-KEMPER, BAYLOR, JOHNSON, LEAH, VAN ROEKEL, LUKE P, McWILLIAMS, JAMES C, SULLIVAN, PETER P, HALL, PAUL S & DONG, JIHAI 2023 Modifying the mixed layer eddy parameterization to include frontogenesis arrest by boundary layer turbulence. *Journal of Physical Oceanography* **53** (1), 323–339.
- CAPET, XAVIER, MCWILLIAMS, JAMES C, MOLEMAKER, M JEROEN & SHCHEPETKIN, ALEXANDER F 2008a Mesoscale to submesoscale transition in the california current system. part i: Flow structure, eddy flux, and observational tests. *Journal of physical oceanography* **38** (1), 29–43.
- CAPET, XAVIER, MCWILLIAMS, JAMES C, MOLEMAKER, M JEROEN & SHCHEPETKIN, ALEXANDER F 2008b Mesoscale to submesoscale transition in the california current system. part iii: Energy balance and flux. *Journal of Physical Oceanography* **38** (10), 2256–2269.
- DAUHAJRE, DANIEL P, SRINIVASAN, KAUSHIK, MOLEMAKER, M JEROEN, GULA, JONATHAN, HYPOLITE, DELPHINE, MCWILLIAMS, JAMES C, BARKAN, ROY & YOUNG, WILLIAM R 2025 Vertical mixing can both induce and inhibit submesoscale frontogenesis. *Journal of Physical Oceanography*.
- DONG, JIHAI, FOX-KEMPER, BAYLOR, ZHANG, HONG & DONG, CHANGMING 2020 The scale of submesoscale baroclinic instability globally. *Journal of Physical Oceanography* **50** (9), 2649–2667.
- EADY, ERIC T 1949 Long waves and cyclone waves. *Tellus* **1** (3), 33–52.
- ELDEVIK, TOR & DYSTHE, KRISTIAN B 2002 Spiral eddies. *Journal of Physical Oceanography* **32** (3), 851–869.
- ELIASSEN, ARNT 1983 The charney-stern theorem on barotropic-baroclinic instability. *pure and applied geophysics* **121**, 563–572.
- Fox-Kemper, Baylor, Ferrari, Raffaele & Hallberg, Robert 2008 Parameterization of mixed layer eddies. part i: Theory and diagnosis. *Journal of Physical Oceanography* **38** (6), 1145–1165.
- GENT, PR 1974 Baroclinic instability of a slowly varying zonal flow. *Journal of Atmospheric Sciences* **31** (8), 1983–1994.
- GULA, JONATHAN, MOLEMAKER, M JEROEN & MCWILLIAMS, JAMES C 2014 Submesoscale cold filaments in the gulf stream. *Journal of Physical Oceanography* **44** (10), 2617–2643.
- HOSKINS, BJ, DRAGHICI, I & DAVIES, HC 1978 A new look at the ω -equation. *Quarterly Journal of the Royal Meteorological Society* **104** (439), 31–38.
- HOSKINS, BRIAN J & BRETHERTON, FRANCIS P 1972 Atmospheric frontogenesis models: Mathematical formulation and solution. *Journal of the atmospheric sciences* **29** (1), 11–37.
- HOSKINS, BRIAN J, MCINTYRE, MICHAEL E & ROBERTSON, ANDREW W 1985 On the use and significance of isentropic potential vorticity maps. *Quarterly Journal of the Royal Meteorological Society* **111** (470), 877–946.
- IOANNOU, PETROS & LINDZEN, RICHARD S 1986 Baroclinic instability in the presence of barotropic jets. *Journal of Atmospheric Sciences* **43** (23), 2999–3014.
- JAMES, IN & GRAY, LJ 1986 Concerning the effect of surface drag on the circulation of a baroclinic planetary atmosphere. *Quarterly Journal of the Royal Meteorological Society* **112** (474), 1231–1250.
- JAMES, IAN N 1987 Suppression of baroclinic instability in horizontally sheared flows. *Journal of Atmospheric Sciences* **44** (24), 3710–3720.
- JONES, WALTER L 1967 Propagation of internal gravity waves in fluids with shear flow and rotation. *Journal of Fluid Mechanics* **30** (3), 439–448.
- KLEIN, PATRICE, LAPEYRE, GUILLAUME, SIEGELMAN, LIA, QIU, BO, FU, LEE-LUENG, TORRES, HECTOR, SU,

- ZHAN, MENEMENLIS, DIMITRIS & LE GENTIL, SYLVIE 2019 Ocean-scale interactions from space. *Earth and Space Science* **6** (5), 795–817.
- MAHADEVAN, AMALA 2016 The impact of submesoscale physics on primary productivity of plankton. *Annual review of marine science* **8** (1), 161–184.
- MASLOWE, SHERWIN A 1986 Critical layers in shear flows. *Annual review of fluid mechanics* **18**, 405–432.
- MCINTYRE, MICHAEL E 1970 On the non-separable baroclinic parallel flow instability problem. *Journal of Fluid Mechanics* **40** (2), 273–306.
- McWILLIAMS, JAMES C 2016 Submesoscale currents in the ocean. *Proceedings of the Royal Society A: Mathematical, Physical and Engineering Sciences* **472** (2189), 20160117.
- McWILLIAMS, JAMES C, GULA, JONATHAN, MOLEMAKER, M JEROEN, RENAULT, LIONEL & SHCHEPETKIN, ALEXANDER F 2015 Filament frontogenesis by boundary layer turbulence. *Journal of Physical Oceanography* **45** (8), 1988–2005.
- MILES, JOHN W 1961 On the stability of heterogeneous shear flows. *Journal of Fluid Mechanics* **10** (4), 496–508.
- MOORE, GW KENT & PELTIER, WR 1987 Cyclogenesis in frontal zones. *Journal of Atmospheric Sciences* **44** (2), 384–409.
- MOORE, GW KENT & PELTIER, WR 1990 Nonseparable baroclinic instability. part ii: Primitive-equations dynamics. *Journal of Atmospheric Sciences* **47** (10), 1223–1242.
- NAKAMURA, NOBORU 1988 Scale selection of baroclinic instability—effects of stratification and nongeostrophy. *Journal of Atmospheric Sciences* **45** (21), 3253–3268.
- OU, HSIEN WANG 1984 Geostrophic adjustment: A mechanism for frontogenesis. *Journal of Physical Oceanography* **14** (6), 994–1000.
- ÖZGÖKMEN, TAMAY M, POJE, ANDREW C, FISCHER, PAUL F & HAZA, ANGELIQUE C 2011 Large eddy simulations of mixed layer instabilities and sampling strategies. *Ocean Modelling* **39** (3-4), 311–331.
- PEDLOSKY, JOSEPH 2013 *Geophysical fluid dynamics*. Springer Science & Business Media.
- POLIZZI, ERIC 2009 Density-matrix-based algorithm for solving eigenvalue problems. *Physical Review B—Condensed Matter and Materials Physics* **79** (11), 115112.
- ROSSBY, CARL-GUSTAF 1937 On the mutual adjustment of pressure and velocity distributions in certain simple current systems. *Journal of Marine Research* **1** (1), 15–28.
- SCHUBERT, RENÉ, GULA, JONATHAN, GREATBATCH, RICHARD J, BASCHEK, BURKARD & BIASTOCH, ARNE 2020 The submesoscale kinetic energy cascade: Mesoscale absorption of submesoscale mixed layer eddies and frontal downscale fluxes. *Journal of Physical Oceanography* **50** (9), 2573–2589.
- SRINIVASAN, KAUSHIK, BARKAN, ROY & McWILLIAMS, JAMES C 2023 A forward energy flux at submesoscales driven by frontogenesis. *Journal of Physical Oceanography* **53** (1), 287–305.
- STONE, PETER H 1966 On non-geostrophic baroclinic stability. *Journal of Atmospheric Sciences* **23** (4), 390–400.
- STONE, PETER H 1970 On non-geostrophic baroclinic stability: Part ii. *J. Atmos. Sci* **27** (5), 721–726.
- STONE, PETER H 1971 Baroclinic stability under non-hydrostatic conditions. *Journal of Fluid Mechanics* **45** (4), 659–671.
- SULLIVAN, PETER P & McWILLIAMS, JAMES C 2018 Frontogenesis and frontal arrest of a dense filament in the oceanic surface boundary layer. *Journal of Fluid Mechanics* **837**, 341–380.
- SULLIVAN, PETER P & McWILLIAMS, JAMES C 2024 Oceanic frontal turbulence. *Journal of Physical Oceanography* **54** (2), 333–358.
- TAYLOR, JOHN R & THOMPSON, ANDREW F 2023 Submesoscale dynamics in the upper ocean. *Annual Review of Fluid Mechanics* **55**, 103–127.
- TEED, ROBERT J, JONES, CHRIS A & HOLLERBACH, RAINER 2010 Rapidly rotating plane layer convection with zonal flow. *Geophysical and Astrophysical Fluid Dynamics* **104** (5–6), 457–480.
- THEOFILIS, VASSILIOS 2011 Global linear instability. *Annual Review of Fluid Mechanics* **43** (1), 319–352.
- THOMAS, LEIF N 2005 Destruction of potential vorticity by winds. *Journal of physical oceanography* **35** (12), 2457–2466.
- THOMAS, LEIF N, TANDON, AMIT & MAHADEVAN, AMALA 2008 Submesoscale processes and dynamics. *Ocean modeling in an Eddying Regime* **177**, 17–38.
- THORPE, AJ, HOSKINS, BJ & INNOCENTINI, V 1989 The parcel method in a baroclinic atmosphere. *J. Atmos. Sci* **46**, 1274–1284.
- TREFETHEN, LLOYD N 2000 *Spectral methods in MATLAB*. SIAM.
- VALLIS, GEOFFREY K 2017 *Atmospheric and oceanic fluid dynamics*. Cambridge University Press.

WANG, TAO, BARKAN, ROY, McWILLIAMS, JAMES C & MOLEMAKER, M JEROEN 2021 Structure of submesoscale fronts of the mississippi river plume. *Journal of Physical Oceanography* **51** (4), 1113–1131.

YU, XIAOLONG, BARKAN, ROY & NAVEIRA GARABATO, ALBERTO C 2024 Intensification of submesoscale frontogenesis and forward energy cascade driven by upper-ocean convergent flows. *Nature Communications* **15** (1), 9214.